AD-A161 124 WIND TUNNEL CALIBRATION OF A PMS (PARTICLE MEASURING SYSTEMS) CANISTER IN (U) NATIONAL AERONAUTICAL ESTABLISHMENT OTTAWA (ONTARIO) J I MACPHERSON SEP 85 1/1

UNCLASSIFIED NAE-AN-32 NRC-24922 F/G 20/6 NL

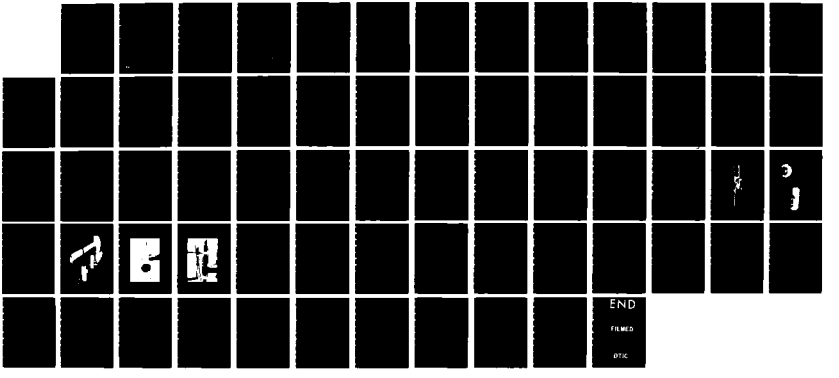

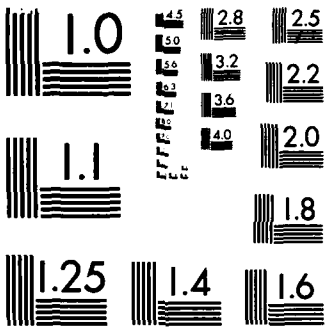

MICROCOPY RESOLUTION TEST CHART
NATIONAL BUREAU OF STANDARDS-1963-A

UNLIMITED
UNCLASSIFIED

Canada

WIND TUNNEL CALIBRATION OF A PMS CANISTER INSTRUMENTED FOR AIRFLOW MEASUREMENT

by

J.I. MacPherson
National Aeronautical Establishment

OTTAWA
SEPTEMBER 1985

ERONAUTICAL NOTE
NAE-AN-32
NRC NO. 24922

National Research Council Canada
Conseil national de recherches Canada

NATIONAL AERONAUTICAL ESTABLISHMENT

SCIENTIFIC AND TECHNICAL PUBLICATIONS

AERONAUTICAL REPORTS:

Aeronautical Reports (LR): Scientific and technical information pertaining to aeronautics considered important, complete, and a lasting contribution to existing knowledge.

Mechanical Engineering Reports (MS): Scientific and technical information pertaining to investigations outside aeronautics considered important, complete, and a lasting contribution to existing knowledge.

AERONAUTICAL NOTES (AN): Information less broad in scope but nevertheless of importance as a contribution to existing knowledge.

LABORATORY TECHNICAL REPORTS (LTR): Information receiving limited distribution because of preliminary data, security classification, proprietary, or other reasons.

Details on the availability of these publications may be obtained from:

Publications Section,
National Research Council Canada,
National Aeronautical Establishment,
Bldg. M-16, Room 204,
Montreal Road,
Ottawa, Ontario
K1A 0R6

ÉTABLISSEMENT AÉRONAUTIQUE NATIONAL

PUBLICATIONS SCIENTIFIQUES ET TECHNIQUES

RAPPORTS D'AÉRONAUTIQUE

Rapports d'aéronautique (LR): Informations scientifiques et techniques touchant l'aéronautique jugées importantes, complètes et durables en termes de contribution aux connaissances actuelles.

Rapports de génie mécanique (MS): Informations scientifiques et techniques sur la recherche externe à l'aéronautique jugées importantes, complètes et durables en termes de contribution aux connaissances actuelles.

CAHIERS D'AÉRONAUTIQUE (AN): Informations de moindre portée mais importantes en termes d'accroissement des connaissances.

RAPPORTS TECHNIQUES DE LABORATOIRE (LTR): Informations peu disséminées pour des raisons d'usage secret, de droit de propriété ou autres ou parce qu'elles constituent des données préliminaires.

Les publications ci-dessus peuvent être obtenues à l'adresse suivante:

Section des publications
Conseil national de recherches Canada
Établissement aéronautique national
Im. M-16, pièce 204
Chemin de Montréal
Ottawa (Ontario)
K1A 0R6

UNLIMITED
UNCLASSIFIED

WIND TUNNEL CALIBRATION OF A PMS CANISTER INSTRUMENTED FOR AIRFLOW MEASUREMENT

ÉTALONNAGE EN SOUFFLERIE D'UNE NACELLE PMS MUNIE D'INSTRUMENTS DE MESURE DU MOUVEMENT DE L'AIR

by/par

J.I. MacPherson

National Aeronautical Establishment

OTTAWA
SEPTEMBER 1985

AERONAUTICAL NOTE
NAE-AN-32
NRC NO. 24922

S.R.M. Sinclair, Head/Chef
Flight Research Laboratory/
Laboratoire de recherche en vol

G.M. Lindberg
Director/Directeur

SUMMARY

Measurements of cloud particle images and concentrations using laser spectrometers housed in pods mounted on the wings or fuselages of research aircraft can be affected by the distortion of the airflow about the aircraft. The Flight Research Laboratory has developed a pod with a Rosemount 858 5-hole probe and pressure transducers to measure airflow angles and velocities at typical mounting locations on cloud physics research aircraft. This report documents the results of an extensive wind tunnel calibration of this pod to determine the factors relating the differential pressure measurements to the flow angles and velocities, and in particular to account for the effects of the canister itself on these measurements.

RÉSUMÉ

Les mesures d'images et de concentrations de particules de nuage au moyen de spectomètres à laser logés dans des nacelles montées sur les ailes ou le fuselage d'aéronefs de recherche peuvent être biaisées par des perturbations du mouvement de l'air autour de l'aéronef. Le Laboratoire de recherche en vol a mis au point une nacelle munie d'une sonde Rosemount 858 à 5 trous et de transducteurs de pression pour mesurer les angles et les vitesses des mouvements de l'air en des points types sur un aéronef de recherche sur la physique des nuages. Ce rapport décrit les résultats d'un essai poussé d'étalonnage en soufflerie de cette nacelle visant à établir une relation entre les mesures de pression différentielle et les angles et vitesses des mouvements de l'air, et à expliquer notamment les effets du récipient lui-même sur ces mesures.

TABLE OF CONTENTS

LIST OF TABLES

LIST OF FIGURES

SYMBOLS

Symbol	Definition
$a_o \ldots a_j$	coefficients in least squares regression analysis
A	a constant based on canister dimensions
C_p	pressure coefficient
k	sensitivity factor relating flow angle to pressure ratio
L	half length of the canister
M	Mach number
P	air pressure
Pd_y	dynamic pressure measured by the probe
P_S	static pressure
P_T	total pressure
P_α	differential pressure between the orifices used for angle of attack measurement
P_β	differential pressure between the orifices used for angle of sideslip measurement
P_γ	static pressure on the surface of a sphere at angle γ to the free stream velocity vector
P_∞	ambient pressure
Q	dynamic pressure; wind tunnel dynamic pressure
R	radius of the spherical nose of the canister
U	free stream velocity; aircraft true airspeed
v	velocity measured by the probe
$x_1 \ldots x_j$	estimated values of parameters in regression analysis
Δx	longitudinal distance ahead of the nose of the canister
Δx_p	longitudinal distance between the canister nose and the static pressure ports on the probe
Δx_{sp}	longitudinal distance between the canister nose and the sampling plane of a PMS 2D-C probe
$y_1 \ldots y_j$	true values of parameters in regression analysis
α	angle of attack
β	angle of sideslip
γ	angle between the free stream velocity vector and any point on the spherical nose of the probe
θ	angle between the longitudinal axis of the probe and the orifices used for flow angle pressure measurement

ξ	non-dimensional distance, $1 + \Delta x/L$
ρ	air density
σ	root-mean-square value
ϕ	angle of probe misalignment in roll axis

Subscripts

i	incompressible
m	measured
o	theoretical

1.0 INTRODUCTION

Most aircraft used in cloud physics research carry laser spectrometers externally mounted on the fuselage or wings to measure concentrations of aerosols, cloud droplets and precipitation particles. Two of these probes (manufactured by Particle Measuring Systems (PMS) in Boulder, Colorado) can also be used to record particle images in the size ranges 25-300 μm (2D-C) and 200-6500 μm (2D-P). In the cloud physics research community there has been a growing interest in the effects of airflow distortion, caused by the aircraft and the pods housing the spectrometers, on the concentrations and images measured by these sensors. A workshop convened to address the broader topic of "The Effects of Airflow Distortion on Aircraft Measurements" was held at the National Center for Atmospheric Research in December, 1983 (Baumgardner, 1984). It was concluded that airborne measurements can be significantly affected by aerodynamic interference depending on the mounting location on the aircraft and the parameter being measured, and that these effects are often subtle and difficult to quantify. The scientific community must give greater attention to these considerations when instrumenting aircraft and using the resulting data.

The National Aeronautical Establishment (NAE) and the Atmospheric Environment Service of Canada (AES) have cooperated for ten years to develop the NAE Twin Otter as a cloud physics research aircraft (MacPherson et al, 1981, Isaac et al, 1982). The aircraft contains instrumentation to measure and record atmospheric state parameters and air motion, and carries four AES-owned PMS probes mounted on pylons under the wings (Fig. 1). The effect of aerodynamic interference on these probes was addressed in a report by Drummond, 1977, followed by a study of the possibility of contamination of the measurements by droplets or ice particles thrown from the propellers (Drummond, 1983). More recently a theoretical model for the flow about the Twin Otter wing was developed that permitted prediction of the flow velocities and angles anywhere ahead of the wing quarter chord point,

and in particular ahead of the PMS canisters (Drummond and MacPherson, 1984). The velocity predictions of the model were verified experimentally by fitting a standard long PMS canister with pitot and static probes and pressure transducers, and making airspeed measurements at each wing mounting location over a wide range of flight conditions. The verified model was used to calculate droplet trajectories on their approach to the probes in order to develop methods to correct droplet images and concentrations for aerodynamic effects (Drummond, 1984, Drummond and MacPherson, 1985).

There is evidence from aircraft with wingtip mounted PMS probes that changing flow angles due to formation of the trailing vortices may be causing distortion of PMS images (Baumgardner, 1984). There is also considerable interest in verifying the flow angles predicted by the theoretical model for flow about the Twin Otter wing; the original pitot/static equipped canister was only capable of speed measurement. Consequently, the canister has now been fitted with a Rosemount 858 5-hole probe and four pressure transducers to measure airspeed, static pressure and the angles of attack (α) and sideslip (β). These measurements can be made near the normal sampling plane of a 2D-C PMS probe or, using a special extension, three feet ahead of the PMS canister. An extensive wind tunnel calibration of this device has been performed to determine the factors relating the differential pressure measurements to flow angles and velocities, and, in particular, the effects of the canister itself on these factors. This report presents the results of the wind tunnel calibration.

It is expected that this specially equipped pod will be flown on the Twin Otter and several other cloud physics aircraft to measure flow velocities and angles at PMS mounting locations under wings, at wingtips and on fuselages. This report will serve as a reference for those studies by describing the pod and documenting the calibration factors necessary for its use.

2.0 THE ROSEMOUNT 858 EQUIPPED CANISTER

A standard PMS long canister (32½") has been fitted with a Rosemount 858* airspeed and flow angle sensor (Fig. 2). In the 'short' configuration, the tip of the probe is 7.07 inches ahead of the spherical nose of the canister (Fig. 3). This is about ½" behind the position of the tips of a 2D-C PMS probe, and about 1¼" ahead of its laser sampling plane. This arrangement was dictated by structural considerations and the desire for a reasonable spacing between the canister and the static pressure holes on the 858 head. This configuration will permit in-flight flow measurements at a position representative of the actual sampling plane. A procedure will be developed below to correct airspeed measurements to the laser sampling plane position.

Flow ahead of the PMS probes is of considerable interest also, for it is here that the aerodynamic forces can influence particle trajectories prior to their arrival at the sampling plane. Therefore, a second configuration has been developed which employs a 30-inch extension between the canister and the 858 head (Figs. 3 and 4). This extended configuration will permit airflow measurement on the Twin Otter ahead of the wing leading edge where large longitudinal gradients in flow angle of attack can be expected. These tests will provide an additional test for the airflow model given by Drummond and MacPherson, 1984.

Aircraft angles of attack and sideslip are currently measured on the Twin Otter by swiveling vanes mounted on a noseboom which also houses a conventional pitot/static probe. The vanes are subject to icing problems during flight in supercooled cloud. It is planned to replace the vanes and the pitot/static probe on the boom with a Rosemount 858 sensor with a deicing capability. Prior to this installation, however, it was considered desirable to test the 858 probe in a wind tunnel to investigate its accuracy in sensing airspeed and static pressure, and to confirm the factors relating flow angle to the measured differential pressures. The 30-inch extension provides adequate spacing from the canister to allow wind tunnel testing of the probe virtually out of the aerodynamic influence of the blunt nose of the canister, thereby simulating its installation on the noseboom.

---

*The name 'Rosemount 858' will sometimes be shortened to '858' in the following text.

Figure 3 is a schematic diagram of the 858-equipped canister giving the principal dimensions for the short and extended configurations. Note that the static pressure orifices are 3.49 inches behind the nose of the probe, and, in the short configuration, only 3.58 inches ahead of the spherical nose of the pod. Dynamic pressure (airspeed) is measured by the pressure difference between the central orifice on the nose of the probe and the static pressure holes. As will be shown in Section 3.3, in the short configuration the static pressure will be influenced by the blunt nose of the canister, resulting in an underestimated airspeed measurement. One of the aims of the wind tunnel tests was to determine the relationship between the measured and true dynamic pressures for later use on the aircraft.

The wind tunnel tests were accomplished using canister-mounted pressure transducers that were already available at the Flight Research Laboratory and covering the flight envelope of the Twin Otter (145 knots indicated airspeed). Table 1 lists the manufacturers' specifications for these transducers. Subsequent to the tunnel tests and prior to flight, it was decided to acquire new differential pressure transducers with at least double the range, so that a single assemblage of transducers could be flown on all potential test aircraft (up to 290 knots IAS). Specifications for these transducers are also given in Table 1. Figure 2 shows the pod fitted with the higher range capsules for the flight configuration.

3.0 THEORY

3.1 Factor Relating Flow Angle to Differential Pressure

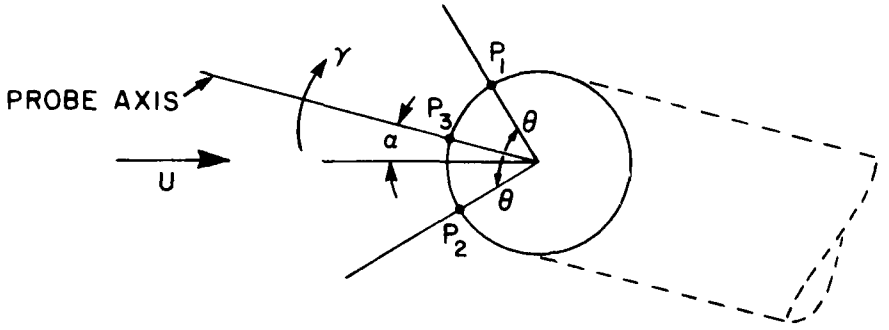

The hemispherical head of the Rosemount 858 probe has a large central orifice to sense total pressure and four smaller pressure taps

TABLE 1. SPECIFICATION OF PRESSURE TRANSDUCERS IN POD

Parameter	Sensor Type	Range (psf)	Operating Accuracy
FOR TUNNEL TESTS			
Ps	CIC 6100 Ser. 4650385	0 - 2160	±0.5% Rep. ±0.05%
Pd_y	Rosemount 831L3 Ser. 53	-72 to 72	±0.5% Rep. ±0.01% Hysteresis ±0.015%
P_α	Rosemount 1221 F1VL5A1A Ser. 1334	-72 to 72	±0.37% Rep. ±0.02% Hysteresis ±0.04%
P_β	" Ser. 1319	"	"
FOR FLIGHT TESTS			
Ps	CIC 6100 Ser. 4650385	0 - 2160	±0.5% Rep. ±0.05%
Pd_y	Rosemount 1221 F2VL7A1AEP5 Ser. 140	-288 to 288	±0.30% Rep. ±0.02%
P_α	Rosemount 1221 F2VL7A1A Ser. 162	-144 to 144	±0.30% Rep. ±0.02%
P_β	" Ser. 163	"	"

drilled at 45 degrees to the probe axis to measure flow angles (Fig. 2). For moderate flow angles, the pressures can be predicted using potential flow theory applied to the forward half of a sphere. In high Reynold's Number uniform flow past a sphere, the static pressure distribution over the surface of a sphere is given by Streeter, 1971:

$$P_\gamma - P_\infty = \tfrac{1}{2}\ \rho U^2\left(1 - \frac{9}{4}\sin^2\gamma\right) \tag{1}$$

where γ is the angle between U and a point on the sphere.
At each of two ports on the sphere at angle θ from the central orifice, and with the flow at an angle of attack α, the pressures are given by:

$$P_1 - P_\infty = \tfrac{1}{2}\ \rho U^2\left(1 - \frac{9}{4}\sin^2(\theta+\alpha)\right) \tag{2}$$

and

$$P_2 - P_\infty = \tfrac{1}{2}\ \rho U^2\left(1 - \frac{9}{4}\sin^2(\theta-\alpha)\right) \tag{3}$$

The pressure difference (P_α) between the two ports is:

$$\frac{P_\alpha}{Q} = \frac{P_2 - P_1}{\frac{1}{2}\rho U^2} = \frac{9}{4}\left(\sin^2(\theta+\alpha) - \sin^2(\theta-\alpha)\right) \tag{4}$$

$$= \frac{9}{4}\sin 2\alpha \sin 2\theta \tag{5}$$

where Q represents the dynamic pressure.
To give the maximum sensitivity to α, $\theta = \pi/4$ so that:

$$\frac{P_\alpha}{Q} = \frac{9}{4}\sin 2\alpha \tag{6}$$

and

$$\alpha = \tfrac{1}{2}\ \sin^{-1}\left(\frac{4}{9}\frac{P_\alpha}{Q}\right) \tag{7}$$

For small angles (7) can be expanded in a series to give:

$$\alpha = \frac{2}{9}\left(\frac{P_\alpha}{Q}\right) + \frac{16}{2187}\left(\frac{P_\alpha}{Q}\right)^3 + \frac{64}{98415}\left(\frac{P_\alpha}{Q}\right)^5 + \ldots \tag{8}$$

A sensitivity factor k_o is usually defined so that:

$$\alpha = k_o^{-1} \left(\frac{P_\alpha}{Q}\right) \tag{9}$$

Using only the first term from (8) and converting α to degrees gives:

$$k_o = 0.0785 \tag{10}$$

This is the value of k_o normally used for this probe for flight at low Mach Numbers. The error in using only the first term in the expansion is 2% for $|\alpha| < 10°$ and <5% for $|\alpha| < 15°$.

The tunnel tests were designed to confirm the sensitivity factor k_o by using the extended probe configuration, and to investigate changes in its value for the short configuration caused by the presence of the blunt nose of the canister.

3.2 Dynamic Pressure

A particular concern in replacing the conventional pitot/static probe on the Twin Otter with the 5-hole sensor is the potential sensitivity of the pressure measurements to flow angle. Conventional pitot probes are relatively insensitive to flows at an angle to the longitudinal axis of the probe, with errors of less than one percent of dynamic pressure even at angles of 20° (Ower and Pankhurst, 1977). On the 5-hole probe, the dynamic pressure is measured between the central orifice on the nose of the probe (P_3) and the static pressure holes 3.49" behind the tip. Even at small off-axis flow angles the stagnation point will be displaced from the central orifice, and the resultant pressure at the central orifice would be expected to be:

$$\frac{P_3 - P_\infty}{\frac{1}{2}\rho U^2} = 1 - \frac{9}{4}\sin^2\alpha \tag{11}$$

Dynamic pressure could be expected to be in error by up to one percent for flow angles of only 4 degrees, and up to 15 percent at flow angles of 15 degrees. The second main objective of the wind tunnel tests, therefore, was to investigate this effect and determine correction factors, if required. An approximate theoretical correction expression is developed in Appendix A which gives:

$$P_T - P_S \approx Pd_y \left[1 + \frac{16}{81}\left(\frac{P_\alpha}{Pd_y}\right)^2 + \frac{16}{81}\left(\frac{P_\beta}{Pd_y}\right)^2\right]^{\frac{1}{2}} \qquad (12)$$

where Pd_y is the measured dynamic presssure $P_3 - P_S$, and P_α and P_β are the differential pressures for the angles of attack and sideslip.

3.3 Canister Effects

Airspeed is derived from the differential pressure measured between the central orifice on the Rosemount probe and its static pressure ports. Since the total pressure is essentially constant along streamlines, the airspeed can be considered to be measured at the location of the static pressure ports. In the short configuration these are only 3.58 inches ahead of the spherical nose of the canister, a position where the static pressure P_S will be elevated above the free stream value P_∞ because of the aerodynamic influence of the blunt nose of the canister. The measured airspeed will therefore be lower than the airspeed that would exist in the absence of the canister. The tunnel tests were designed to determine correction factors relating the measured dynamic pressure Pd_y to the true values, and to compare the results with theoretical calculations for this effect.

Three different theoretical expressions have been derived to predict the effect of the canister on the measured airspeed and dynamic pressure. The canister was modeled as a sphere, as a simple source and as a Rankine body in a uniform flow field. The derivations appear in Appendix B by A.M. Drummond with the resulting equations reproduced below. The expressions are applicable for velocity prediction ahead of the canister along its axis of symmetry.

Modeling the canister as a sphere, the predicted measured-to-free-stream velocity ratio is given by:

$$\frac{v}{U} = \left\{1 - \frac{1}{\left(1 + \frac{\Delta x}{R}\right)^3}\right\} \qquad (13)$$

where R is the radius of the spherical nose of the canister and Δx is the longitudinal distance ahead of the canister. The simple source model gives:

$$\frac{v}{U} = \left\{1 - \frac{1}{\left(1 + \frac{2\Delta x}{R}\right)^2}\right\} \tag{14}$$

The sphere model has no cylindrical section and the source model has infinite length. A Rankine body has a finite length and a nearly cylindrical centre section as well as a blunt nose, although not as blunt as a sphere. The hemispherical end of the canister has a diameter of 7 inches while the cylindrical portion has a diameter of 6.5 inches with an overall length of 32½ inches. The Rankine body can never account for the discontinuity where the hemisphere meets the cylinder. From Appendix B, the Rankine Body model for the canister gives the following velocity ratio:

$$\frac{v}{U} = 1 - \frac{0.03684\ \xi}{(\xi^2 - A^2)^2} \tag{15}$$

where $\xi = 1 + \frac{\Delta x}{L}$; A = 0.8989 and L is the half length of the pod (16.25 inches).

All three models of the canister exhibit an axial velocity defect which is a decreasing function of distance from the nose. Table 2 presents the velocity ratio as a function of Δx for the three models

TABLE 2. PREDICTED VELOCITY RATIOS

Δx inches		Velocity Ratio $\frac{v}{U}$		
		Sphere	Source	Rankine Body
	2.0	0.742	0.782	0.798
short probe	3.58	0.879	0.892	0.903
	4.0	0.898	0.907	0.917
	6.0	0.950	0.949	0.956
	8.0	0.972	0.968	0.973
	10.0	0.982	0.978	0.982
	20.0	0.997	0.994	0.995
extended probe	33.4	0.999	0.998	0.998

using Equations (13), (14) and (15). At distances greater than about 4 inches from the canister nose, the three models give almost identical predictions for the velocity ratio on the longitudinal axis ahead of the canister.

4.0 THE WIND TUNNEL TESTS

The NAE 6 × 9 foot (54.5 ft^2 area) low speed wind tunnel was used for testing the 858-equipped pod. The tunnel is of the closed circuit design and is capable of steady airspeeds up to about 180 knots (Q ≈ 110 psf). The pod was mounted in the centre of the test section upon a specially manufactured 3-foot streamlined pylon, which was in turn attached to the turntable in the floor of the tunnel. Wiring from the transducers was fed through the pylon and through the floor of the tunnel, thereby making an aerodynamically clean test assembly. Figures 5 and 6 show the pod in the tunnel in both its short and extended configurations. The canister was mounted inverted to its normal orientation on the aircraft. Rotation of the well calibrated turntable permitted precise settings of the angle of sideslip β of the probe, with positive β corresponding to right sideslip in the flight configuration. The angle of attack was varied using interchangeable machined spacing collars between the canister and the pylon, which permitted nominal angles of attack of -10, -5, 0, +5 and +10 degrees. Angle of attack was carefully measured with an inclinometer after each collar change.

The resident data acquisition system of the wind tunnel was used to record data from the pod tests. Output signals from the four pressure transducers were fed through amplifiers to analog-to-digital (A/D) converters, in which 15 bits plus sign corresponded to ±10 volts. The digitized pressure data were input to a PDP-1160 processor along with measurements of tunnel Q, turntable angle and tunnel static pressure. At each test point the A/D system sampled the signal from each pressure transducer 240 times in a two second period. The processor computed the mean and RMS value for each pressure, plotted the four average pressures versus β and stored the output data on a

TABLE 3. SUMMARY OF TUNNEL TEST CONDITIONS

Run #	Probe	Nominal Q psf	Ambient P_∞ mb	Temp °C	α deg	β Range deg	Comments
02	short	20 - 70	1003	21.7	0.2	0	Vary Q
04	"	50	"	21.9	"	±14	
05	"	70	"	22.1	"	±10	
07	"	50	1002	22.0	5.3	±14	
08	"	70	"	22.9	"	±10	
10	"	50	"	22.6	10.3	±14	
11	"	70	"	22.6	"	±10	
13	"	50	"	22.5	-4.9	±14	
14	"	70	"	22.7	"	±10	
16	"	50	"	22.9	-9.8	±14	
17	"	70	"	23.4	"	±10	
19	Long	20 - 70	1000	21.9	0.6	0	Vary Q
20	"	35	"	22.2	"	±15	
21	"	45	"	22.3	"	±15	
22	"	55	"	23.9	"	±14	
24	"	35	"	23.0	5.7	±15	
25	"	45	"	23.0	"	±15	
26	"	55	"	23.4	"	±14	
28	"	35	"	23.0	10.8	±15	
29	"	45	"	23.1	"	±15	
30	"	55	"	23.1	"	±14	
32	"	35	"	23.0	-4.4	±15	
33	"	45	"	23.5	"	±15	
34	"	55	"	23.5	"	±14	
36	"	35	"	23.0	-9.4	±15	
37	"	45	"	23.5	"	±15	
38	"	55	"	23.7	"	±14	

disk. These were subsequently written to tape and transferred to the NRC time-shared IBM-3081 computer system for further processing using remote terminals at the Flight Research Laboratory. Figures 7 and 8 illustrate example data output from the wind tunnel data acquisition system. The columns in Fig. 7 represent test point, β, tunnel velocity (fps), P_α (psf), the RMS value from the 240 readings, P_β and its RMS, Pd_y, and the probe and tunnel static pressure differences from ambient (psf).

Prior to installation in the wind tunnel, the four pressure transducers were calibrated at the Flight Research Laboratory in terms of output voltage versus applied pressure. At the tunnel, the capsules were recalibrated through the entire sensor, amplifier, A/D and processor system to produce calibration curves in terms of pressure in psf versus bits. Shown below are the resulting resolutions for each sensor in the tunnel tests and the RMS deviations of the calibrated points from the best-fitting straight lines.

	Resolution psf per bit	RMS psf
P_α	8.67×10^{-3}	2.7×10^{-2}
P_β	8.30×10^{-3}	7.6×10^{-2}
Pd_y	1.00×10^{-2}	1.7×10^{-1}
P_S	1.64×10^{-1}	1.3

Table 3 presents a summary of the test conditions for each of the wind tunnel runs. The probe in its short configuration was first subjected to increasing speeds to Q = 70 psf at zero flow angles, and then was tested at the five angles of attack at nominal tunnel dynamic pressures of 50 and 70 psf. The extended probe was tested at zero α and β to Q = 70 psf, followed by runs with angle variation at nominal dynamic pressures of 35, 45 and 55 psf. Table 4 summarizes the test ranges of speed and angle which approximate the flight envelope of the Twin Otter.

The test limits for β and dynamic pressure were determined by structural considerations for the probe/pylon combination. At high Q, large sideslip angles caused vibration of the 3-foot floor-mounted

pylon. Additional bracing of the pylon was accomplished during the tests, but the limits given above were considered to be adequate to simulate use of the probe on the aircraft.

TABLE 4. TESTED RANGES OF ANGLES AND AIRSPEED

Nominal Q psf	IAS kts	Tested Angle Range Deg.			
		Short		Extended	
		α	β	α	β
20	77	0	0	0	0
30	94	0	0	0	0
35	102	-	-	±10	±15
40	109	0	0	0	0
45	115	-	-	±10	±15
50	121	±10	±14	0	0
55	127	-	-	±10	±14
60	133	0	0	0	0
70	144	±10	±10	0	0

5.0 DATA PROCESSING

A program was written to compute the pressure ratios P_α/Pd_y and P_β/Pd_y for each test case and to plot these variables versus the angles of attack and sideslip. This program also employed the sphere model for the canister effects given in Section 3.3 to estimate the dynamic pressure at the tip of the probe based on the measured Pd_y.

It was anticipated that the angles measured by the probe might not be simple linear functions of the pressure ratios as predicted by Equation (9), particularly in the case of the short probe where the aerodynamic influence of the canister might introduce cross-coupling between the α and β measurements. In a region of distorted flow, P_α, for example, might be a function of not only α but also, to a lesser degree, the sideslip angle β. A program was written utilizing least squares regression techniques to solve for the coefficients a_o to a_j in expressions of the following form:

$$y(i) = a_o + a_1x_1(i) + a_2x_2(i) \ldots + a_jx_j(i) \ , \ i=1 \text{ to } n \qquad (16)$$

where n is the number of test points, y is the 'true' value of a parameter (such as tunnel β) and x_1 to x_j are the various estimators such as the pressure ratios.

6.0 RESULTS

6.1 Airspeed and Dynamic Pressure

As explained in Section 3.3, the airspeed can be considered to be measured on the longitudinal axis of the probe at the station of the static pressure ports. In the short configuration this point is well within the aerodynamic influence of the nose of the canister. Test Runs 02 and 19 (Table 3) were performed with the short and extended probes respectively, with α and β near zero. The tunnel dynamic pressure was varied in 10 psf increments from 20 to 70 psf. Figure 9 presents plots of the measured Pd_y versus tunnel dynamic pressure Q for both configurations. Clearly the canister has a large effect on Pd_y measured by the short probe, but the linearity of the plot indicates that a constant factor can be used to correct Pd_y to true dynamic pressure. The least squares analysis was done for the zero flow angle cases, as well as for all test points (i.e. all speeds, all flow angles). The resulting Pd_y to tunnel Q ratios are given below:

TABLE 5. DYNAMIC PRESSURE AND VELOCITY RATIOS

	Number of test points	α	β	Pd_y/Q	RMS psf	v/U
Extended- Run 19 only	6	0.6	0	0.997	0.01	0.998
- All Runs	251	±10	±15	1.004	0.36	1.002
Short - Run 02 only	6	0.2	0	0.755	0.10	0.869
- All Runs	136	±10	±14	0.789	1.18	0.888

Not surprisingly, the least squares fits, as indicated by the RMS values, are much better for the zero flow angle cases. But for use on the aircraft in flight, there will in general be significant angles of attack and sideslip, so the ratios derived from all the runs should

be used. The RMS errors of 0.36 and 1.18 psf correspond to airspeed accuracies of 0.4 and 1.2 knots at an indicated airspeed of 140 knots. The better accuracy for the extended probe is a reflection of the minimal canister effects in that configuration. Based on these results, it is expected that use of the 5-hole probe on the aircraft noseboom will give airspeeds to an accuracy of about 0.4 knots at the speeds and flow angles experienced by the Twin Otter.

The last column in Table 5 lists the experimental velocity ratios computed from the square root of the pressure ratios Pd_y/Q. These are plotted in Figure 10 versus the distance Δx ahead of the nose of the canister, along with the predicted ratios from Table 2 based on modeling the canister as a sphere, a source and a Rankine Body. The three models give very similar results, and there is little aerodynamic effect due to the canister for Δx greater than about 12 inches. The tunnel test data show very good agreement with the predictions. The sphere model appears to provide the best prediction, and its ease of use also made it the preferred model in studies of the flow ahead of PMS canisters on the Twin Otter wing (Drummond and MacPherson, 1984, 1985).

The above factors relate the measured velocity to the true tunnel velocity. Therefore they can be used to correct the measured Pd_y for canister effects and deduce velocities that would exist in the complete absence of the measuring pod. In considering aerodynamic effects on cloud physics measurements, however, it is the velocity at the laser sampling plane in the presence of the canister that is of major interest. Figure 10 shows that at the sampling plane of a 2D-C probe the velocity will be about 0.95 of the velocity that would exist in the absence of the PMS canister.

The spherical model (Equation (13)) can be used to relate the velocity v_m actually measured by the 858-equipped probe, as derived from Pd_y, to the velocity v_{sp} at the 2D-C sampling plane:

$$\frac{v_{sp}}{v_m} = \frac{1 - \dfrac{1}{\left(1 + \dfrac{\Delta x_{sp}}{R}\right)^3}}{1 - \dfrac{1}{\left(1 + \dfrac{\Delta x_p}{R}\right)^3}} \qquad (17)$$

where R is the radius of the canister nose, and Δx_p and Δx_{sp} are the distances ahead of the canister nose of the static pressure ports on the 858-equipped pod and the laser sampling plane on the 2D-C probe respectively. For the short probe configuration Δx_p = 3.58 and Δx_{sp} = 5.81 inches and the resulting ratio is 1.077.

In summary, when using the short probe to measure velocities that would exist at a 2D-C sampling plane with the PMS pod in place, the measured velocities must be multiplied by 1.077. To estimate the airspeed that would exist at these mounting locations in the complete absence of the PMS canister, the measured velocity must be multiplied by the inverse of the experimental ratio given in Table 5, i.e. 1.0/0.888 = 1.126.

As mentioned in Section 3.2, it was expected that airspeed (dynamic pressure) measured by the 858 probe would be sensitive to flow angles. An expression was developed (Equation 12) utilizing P_α and P_β to correct Pd_y for potential errors. Considerable evidence from the wind tunnel tests shows that this correction is generally unnecessary, especially for the extended probe which is representative of use of the 858 sensor on the aircraft noseboom. The least squares regression analysis using all test points was employed to investigate the α and β effects on airspeed. The following relationships were derived, where Q, the tunnel dynamic pressure, was considered to be correct.

Extended Probe	RMS Deviation psf	
$Q = 0.71 + 0.996\ Pd_y$	0.37	(18)
$Q = 0.71 + 0.996\ Pd_y + 0.0028\ P_\alpha + 0.0\ P_\beta$	0.36	(19)
$Q = 0.63 + 0.999\ Pd_y + 0.0081\ \lvert P_\alpha \rvert + 0.0063 \lvert P_\beta \rvert$	0.34	(20)
Short Probe		
$Q = 0.41 + 1.268\ Pd_y$	1.18	(21)
$Q = 0.34 + 1.269\ Pd_y + 0.0101\ P_\alpha + 0.0018\ P_\beta$	1.13	(22)
$Q = 0.51 + 1.3178\ Pd_y - 0.0389\ \lvert P_\alpha \rvert - 0.0465 \lvert P_\beta \rvert$	0.51	(23)

For the extended probe, the flow angle coefficients are very small and their inclusion produces no significant reduction in the RMS deviations between the measured points and the best-fitting equation. For the short probe, the addition of terms incorporating the absolute values of P_α and P_β improves the regression fit, with the RMS error deviation reduced by about a half. Coefficients for the P_α and P_β terms are 5 to 7 times larger than for the extended case, presumably a result of canister effects. Use of Equation (23) may be preferred to Equation (21) to achieve the best possible airspeed measurements in the short configuration.

An additional check of flow angle effects was conducted by using Equation (12) to compute a corrected Pd_y for each test point. Figure 11 illustrates the corrected and uncorrected dynamic pressures plotted versus β for the extended probe at angles of attack of 0.6, 5.7 and 10.8 degrees. The tunnel speed was approximately 127 knots (Q ≈ 55 psf). It is apparent that the uncorrected Pd_y already adequately matches the tunnel Q at sideslip angles up to at least 12 degrees, even in conjunction with angles of attack up to 10.8 degrees. The inclusion of correction factors based on P_α and P_β is unnecessary and would, in fact, degrade the Pd_y measurements.

6.2 Static Pressure

The results above were somewhat unexpected, since total pressure (and therefore Pd_y) was anticipated to decrease proportionally to the square of the sine of the off-axis flow angle (Equation (11)). Examination of plots of probe static pressure versus β, such as shown in the lower right of Figure 8, reveals that P_S decreases with flow angle in a manner that compensates for total pressure decreases, so that Pd_y is relatively insensitive to flow angle.

In tunnel testing the extended probe, static pressure differences from ambient up to 4.4 psf were measured, generally in cases with high flow angles at the higher airspeeds. This could represent height errors of about 60 feet at sea level and 90 feet at 15,000 feet when the 858 probe is used to measure altitude on the aircraft noseboom. This performance is not as good as that of the conventional static pressure probe currently used on the Twin Otter.

To use the 858-equipped probe on the Twin Otter and other aircraft for studies of airflow effects at PMS mounting locations, the measurement of a highly accurate P_S is not absolutely essential since this measurement will likely be available from another sensor on the aircraft. Space limitations within the test pod dictated the use of a small static pressure transducer which does not have the resolution or the accuracy of the other three transducers in the pod (Section 4.0). Calibration of the static pressure capsule had a RMS deviation of 1.3 psf.

It is in considering the replacement of the conventional pitot/static probe on the noseboom of the Twin Otter that the question of the accuracy of the 858 probe in sensing static pressure becomes important. Since this installation is simulated by the extended configuration in the tunnel tests, the regression analysis was used to relate the measured static pressure P_S to the true value. The best fit was obtained by the following equation:

$$\Delta P_S = P_S - P_\infty = -2.091 + 0.1189\ Pd_y - 0.0800|P_\alpha| - 0.0684|P_\beta| \qquad (24)$$

with an RMS deviation of 0.9 psf. The corrected P_∞ could be deduced from this equation to an accuracy of about one psf, which is of the same order as the accuracy of the calibration of the transducer. When used on the noseboom of the aircraft, there are other position errors associated with the blunt nose of the aircraft and upwash ahead of the wing. Therefore, after installation on the aircraft, another expression of the form of Equation (24), but with different coefficients, must be derived from flight test data using a trailing cone or a tower-measured static pressure as a reference.

6.3 Flow Angles

The theoretical considerations given in Section 3.1 indicate that, for small flow angles, the differential pressure measurements P_α and P_β can be expected to be linearly related to flow angle in the form $P_\beta/Q = k_o\beta$. For each test run, that is at each combination of tunnel Q and angle of attack, P_β/Pd_y was calculated and plotted versus sideslip angle β. The least squares procedure was used to solve for the

experimental sensitivity factor k_m for each run. Table 6 summarizes these results, and includes the correlation coefficient (CC) for the fitted straight line and the RMS deviation of the fit in terms of pressure ratio and angle. Figure 12 presents plots of P_β/Pd_y versus β for the extended probe. Each frame gives results for a single angle of attack and has superimposed data points and fitted straight lines for the three test values of tunnel Q, nominally 35, 45 and 55 psf. This figure and Table 6 show that there is little variation in the measured sensitivity factor k_m with Q or with α. RMS levels for the individual fits are small, corresponding to 0.06 to 0.15 degrees in β.

Results for the short probe configuration are given a similar presentation in Figure 13, with each frame containing plots from the two test dynamic pressures of 50 and 70 psf. Here there is a discernible difference in the slopes for the two test velocities, with Table 6 showing that k_m increases slightly with dynamic pressure. At Q = 70 psf, the tested β range was limited to ± 10 degrees because of the onset of vibration of the probe/pylon combination at higher sideslip angles. The plotted crosses are well represented by a linear fit with RMS deviations equivalent to angles of 0.07 to 0.13 degrees. For Q = 50 psf, the plotted triangles diverge somewhat from the best straight line at angles above ± 10 degrees. The resultant RMS levels fall in the range 0.12 to 0.27 degrees, still an acceptable fit.

In Figure 14 the test results for the extended probe at all five angles of attack are combined in single plots. Frames (a), (b) and (c) give the plotted points and best fitting straight lines for the nominal tunnel Q of 35, 45 and 55 psf respectively. Scatter in the combined data is modest, as indicated by only slight offsets of the overlapping circles representing individual test points. The data are well fitted by straight lines, the slopes of which are given in Lines 16 to 18 in Table 6. Figure 14(d) presents data from all 245 test points, i.e. for all velocities and all angles of attack. The linear fit gives $k_m = 0.07800$ with an overall RMS level equivalent to 0.18 degrees (Line 19, Table 6).

Figure 15 gives a similar presentation of the results from the short probe configuration. An average sensitivity factor of k_m = 0.1001 with an RMS of 0.33 degrees applies when data from all 130 test points are combined (Line 32, Table 6). The increased scatter in the data for the short probe is likely a reflection of the aerodynamic influence of the canister. Nevertheless, the wind tunnel results suggest that, for each probe configuration, the use of a single k_m for all angles of attack and all values of Q covering the Twin Otter's speed range will be acceptable for flow angle accuracy of 0.18 and 0.33 degrees for the extended and short probes respectively.

The difference between the sensitivity factors for the extended and short probes appears to be due entirely to the effect of the canister on the measured dynamic pressure Pd_y. The expression for the measured sensitivity factor can be expanded to give:

$$k_m = \frac{1}{\beta}\left(\frac{P_\beta}{Pd_y}\right) = \frac{1}{\beta}\left(\frac{P_\beta}{Q}\right)\left(\frac{Q}{Pd_y}\right) = k_o\left(\frac{Q}{Pd_y}\right) \qquad (25)$$

where k_o = 0.0785 from the theoretical development (Equation (10)). Using the overall average experimental k_m = 0.1001 for the short probe, the ratio k_m/k_o = 1.275. This agrees to within one percent with dynamic pressure ratio Q/Pd_y of 1.0/0.789 = 1.267 determined in the wind tunnel tests (Table 5). For the extended probe, for which the dynamic pressure ratio is virtually unity (Table 5), the average k_m for all test points of 0.07800 is extremely close to the predicted theoretical value.

If the 858 sensor head were to be mounted at a different distance ahead of the PMS canister, the results above show that the sensitivity factor could be reliably predicted utilizing Equation (25). The pressure ratio Q/Pd_y could be calculated by modeling the canister as a sphere and using the square of the resulting velocity ratio from Equation (13).

TABLE 6. LEAST SQUARES FITS FOR k_m

Line No.	Run(s)	α deg	Q/nom psf	BIAS	k_m	RMS	RMS deg	CC	No. of Test Pts.	Figure
	Extended									
1	36	-9.4	35	-.013	.0779	.0060	.08	.99997	17	12(a)
2	37	"	45	-.014	.0783	.0048	.06	.99998	17	"
3	38	"	55	-.012	.0792	.0063	.08	.99996	15	"
4	32	-4.4	35	-.033	.0772	.0091	.12	.99992	17	12(b)
5	33	"	45	-.034	.0782	.0106	.14	.99990	17	"
6	34	"	55	-.036	.0790	.0117	.15	.99985	15	"
7	20	0.6	35	-.023	.0767	.0058	.08	.99997	17	12(c)
8	21	"	45	-.026	.0771	.0098	.13	.99991	17	"
9	22	"	55	-.024	.0776	.0117	.15	.99985	15	"
10	24	5.7	35	-.006	.0773	.0068	.09	.99996	17	12(d)
11	25	"	45	-.009	.0783	.0070	.09	.99996	17	"
12	26	"	55	-.012	.0790	.0076	.10	.99994	15	"
13	28	10.8	35	-.022	.0778	.0065	.08	.99996	17	12(e)
14	29	"	45	-.019	.0784	.0092	.12	.99993	17	"
15	30	"	55	-.021	.0792	.0049	.06	.99997	15	"
16	{20,24,28, 32,26	ALL	35	-.020	.0774	.0123	.16	.99986	85	14(a)
17	{21,25,39, 33,37	"	45	-.020	.0780	.0130	.17	.99985	85	14(b)
18	{22,26,30, 34,38	"	55	-.023	.0787	.0139	.18	.99979	75	14(c)
19	ALL	ALL	ALL	-.020	.0780	.0140	.18	.99982	245	14(d)
	Short									
20	16	-9.8	50	-.020	.0986	.0156	.16	.99983	15	13(a)
21	17	"	70	-.027	.1014	.0085	.08	.99991	11	"
22	13	-4.9	50	-.055	.0986	.0220	.22	.99967	15	13(b)
23	14	"	70	-.058	.1023	.0135	.13	.99978	11	"
24	4	0.2	50	-.014	.0987	.0268	.27	.99951	15	13(c)
25	5	"	70	-.009	.1023	.0128	.13	.99980	11	"
26	7	5.3	50	.006	.0999	.0237	.24	.99962	15	13(d)
27	8	"	70	.006	.1035	.0130	.13	.99980	11	"
28	10	10.3	50	.014	.0998	.0119	.12	.99990	15	13(e)
29	11	"	70	.010	.1033	.0069	.07	.99994	11	"
30	{4,7,10, 13,16	ALL	ALL	-.014	.0991	.0321	.32	.99930	75	15(a)
31	{5,8,11, 14,17	ALL	ALL	-.016	.1026	.0277	.27	.99909	55	15(b)
32	ALL	ALL	ALL	-.015	.1001	.0326	.33	.99917	130	15(c)

The experimental sensitivity factors k_m averaged for each tunnel speed (Table 6, Lines 16-18 and 30-31) show a slight increase with speed over the tested Mach Number range of 0.15 to 0.22. Plotted data from an in situ calibration of an 858 probe on the National Center for Atmospheric Research Sabreliner showed the same trend for Mach Numbers less than 0.35 (Fig. 4 of Brown et al, 1983). The Prandtl-Glauert Rule (Kuethe and Schetzer, 1950) indicates that at Mach Numbers less than about 0.5, pressure coefficients Cp_m (such as P_β/Q) in compressible flow are related to their incompressible values Cp_i by the expression:

$$\frac{Cp_m}{Cp_i} = \frac{1}{(1 - M^2)^{\frac{1}{2}}} = \frac{k_m}{k_o} \qquad (26)$$

Over the range of Mach Numbers for the wind tunnel tests of the extended probe, a one percent increase in the measured k_m could be expected, which agrees closely with the observed values given in Lines 16-18 of Table 6. In the speed range of the Twin Otter, the resulting variation in the computed flow angles would amount to only 0.1 degree even at angles of 10 degrees. Use of an average k_m and ignoring Mach effects would provide acceptable accuracy.

It is generally assumed that 858-type probes can be used on aircraft nosebooms with negligible cross-coupling between the α and β measurements at flow angles up to at least ±10 degrees (Kaushagen, 1949), i.e. that angles of attack and sideslip can be calculated independently. The tunnel test data were used to investigate this premise for both the extended configuration, which simulates a noseboom installation, and the short configuration, where canister effects might invalidate this assumption. The least squares regression technique (Equation (16)) was used to relate the flow angles to various combinations of parameters in an attempt to determine relationships that would provide even better fits than the simple linear expressions $\beta = k_m^{-1} (P_\beta/Q)$ normally used. Results are presented in Table 7.

Two conclusions can be drawn from the equations for the extended probe. First, the inclusion of additional cross-coupling terms does not improve the fit over use of the simple linear expression given above. The coefficient of the P_α in the β equation is very small, for example, and the RMS deviation of the fit is unchanged. Secondly, the resultant k_m values for the α and β expressions are almost identical and very close to the theoretical value of 0.0785, which confirms the symmetry of the hemispherical end and pressure ports of the probe.

In the case of the short probe, the inclusion of the cross coefficients appears to improve the fit by about 0.1 degrees RMS. Also the k_m for angle of attack is about 5 per cent less than that for sideslip. This latter effect may be a result of an asymmetry in the flow caused by the pylon supporting the canister. However, near the completion of the tunnel testing of the probe in its short configuration, it was discovered that the 858 sensor was improperly aligned in the canister. It had been mounted with a slight counter-clockwise rotation as seen from the front, i.e. the pressure ports measuring α were not perfectly vertical. It was estimated that the misalignment was about 2 degrees.

TABLE 7. REGRESSION ANALYSIS RESULTS FOR FLOW ANGLES

Expression	k_m	RMS	Equation Number
Extended Configuration			
$\beta = 0.260 + 12.8159\ (P_\beta/Pd_y)$	0.0780	0.18	(27)
$\beta = 0.262 + 12.8153\ (P_\beta/Pd_y) - 0.0329\ (P_\alpha/Pd_y)$	0.0780	0.18	(28)
$\beta = 0.229 + 12.8158\ (P_\beta/Pd_y) - 0.0007\ Pd_y$	0.0780	0.18	(29)
$\alpha = -0.076 + 12.7985\ (P_\alpha/Pd_y)$	0.0781	0.25	(30)
$\alpha = -0.080 + 12.8052\ (P_\alpha/Pd_y) + 0.2327\ (P_\beta/Pd_y)$	0.0781	0.19	(31)
Short Configuration			
$\beta = 0.142 + 9.9726\ (P_\beta/Pd_y)$	0.1003	0.32	(32)
$\beta = 0.144 + 9.9699\ (P_\beta/Pd_y) - 0.2756\ (P_\alpha/Pd_y)$	0.1003	0.26	(33)
$\alpha = 0.130 + 10.4232\ (P_\alpha/Pd_y)$	0.0959	0.34	(34)
$\alpha = 0.134 + 10.4272\ (P_\alpha/Pd_y) + 0.3209\ (P_\beta/Pd_y)$	0.0959	0.23	(35)

To examine the effect of this misalignment, consider the flow angles α_m and β_m sensed by the differential pressure transducers as functions of the true α and β and the rotation angle ϕ, such that:

$$\beta_m = \beta \cos\phi + \alpha \sin\phi = \frac{1}{k_m} \frac{P_\beta}{Q} \tag{36}$$

$$\alpha_m = \alpha \cos\phi - \beta \sin\phi = \frac{1}{k_m} \frac{P_\alpha}{Q} \tag{37}$$

Solving these equations for α and β gives:

$$\beta = \frac{1}{k_m} \left(\frac{P_\beta}{Q}\right)\cos\phi - \frac{1}{k_m} \left(\frac{P_\alpha}{Q}\right)\sin\phi \tag{38}$$

$$\alpha = \frac{1}{k_m} \left(\frac{P_\alpha}{Q}\right)\cos\phi + \frac{1}{k_m} \left(\frac{P_\beta}{Q}\right)\sin\phi \tag{39}$$

Note that the signs of the coefficients of the cross terms in Equations (33) and (35) in Table 7 correspond with those in the expressions above. Equating them gives:

$$\frac{-\sin\phi}{k_m} = -0.2756 \text{ or } \frac{\sin\phi}{k_m} = 0.3209 \tag{40}$$

Assuming $k_m = 0.100$ and solving for ϕ, estimates for ϕ of 1.58 and 1.84 degrees are obtained, close to the estimated misalignment observed. It is probable that, had the misalignment not existed, the coefficients of the cross terms would have been negligible and the simple linear relationships in Equations (32) and (34) would provide adequate accuracy. The misalignment had no effect on the determination of the k_m factor from fits of P_β/Pd_y versus β since the cosine of ϕ is essentially 1.0 to within 0.05 percent.

It can be concluded from this work that the α and β flow angles can be calculated independently and that the inclusion of the cross terms is unwarranted. For the extended probe a sensitivity factor of 0.0780 can be used for both α and β, and the RMS error levels in using the linear fit to $\pm$15 degrees will be of the order of 0.18 degrees. For the short probe, a k_m of 0.1001 appears to give the best results with an RMS variation of approximately 0.32 degrees. It is recommended that this value be used for both α and β, although the α fit in Table 7 indicated a lower slope. It must be remembered that during the tunnel tests, α was incremented in 5 degree steps using machined collars, while the tunnel turntable provided accurate β variation in 2 degree steps. The k_m factor deduced from the β expression should therefore be regarded as the more reliable of the two.

7.0 USE OF THE PROBE ON AIRCRAFT

Having been wind tunnel calibrated, the 858-equipped canister will be flown on the NAE Twin Otter and other cloud physics research aircraft to measure airspeed and flow angles at and ahead of PMS probe mounting locations. This section will summarize the best equations and sensitivity factors to be used in airborne tests with this device and present its operational limitations.

7.1 Dynamic Pressure, Airspeed

For the extended probe, $Pd_y = P_3 - P_s$ measured by the probe can be used to calculate airspeed to an accuracy of about 0.4 knots at an indicated airspeed of 140 knots. Since canister effects in this configuration are negligible, measured airflow will be representative of conditions 3 feet ahead of PMS mounting locations both in the presence and absence of the PMS probe itself.

Using the short configuration, the airspeed at the 2D-C sampling plane will be 1.077 times that derived from the dynamic pressure Pd_y measured by the probe. To calculate the airspeed that would exist at the location of the static pressure ports, but in the complete absence of the probe and canister and their effects, either of the following relationships from Section 6.1 can be used for the dynamic pressure:

$$P_T - P_S = 0.41 + 1.268\ Pd_y \qquad (21)$$

σ = 1.18 psf (≈1.2 knots at 140 IAS)

$$P_T - P_S = 0.51 + 1.3178\ Pd_y - 0.0389|P_\alpha| - 0.0465|P_\beta| \qquad (23)$$

σ = 0.51 psf (≈0.6 knots at 140 IAS)

7.2 Static Pressure

As mentioned in Section 6.2, better sources of static pressure for altitude calculation will exist elsewhere on the test aircraft. In the short configuration the pod-measured static pressure will be elevated considerably above ambient due to flow blockage ahead of the canister. In the extended configuration, Section 6.2 gives an expression (Equation (24)) with which to correct the measured P_S using Pd_y, P_α and P_β with a resulting accuracy of about 1 psf.

7.3 Flow Angles

The tunnel tests showed that at flow angles up to at least ±15 degrees, the α and β computations can be handled independently. The flow angles can be treated as linear functions of the measured pressure ratios:

$$\alpha = k_m^{-1}\left(\frac{P_\alpha}{Pd_y}\right) \text{ and } \beta = k_m^{-1}\left(\frac{P_\beta}{Pd_y}\right) \text{ (angles in degrees)} \qquad (41)$$

For Mach Numbers up to at least 0.22, the average values of the sensitivity factor k_m determined from the wind tunnel tests provide acceptable accuracy. These values are 0.0780 for the extended probe and 0.1001 for the short probe, giving RMS accuracies of approximately 0.2 and 0.3 degrees respectively. At higher Mach Numbers, these factors could possibly be corrected using the Prandtl-Glauert Rule by dividing k_m by $(1 - M^2)^{\frac{1}{2}}$.

7.4 Operational Limitations

The differential pressure transducers installed in the canister are limited to 144 psf for flow angle and 288 psf for airspeed. During the flight tests, considerable care must be taken not to exceed these limits. The following table gives the flow angle limitations versus indicated airspeed.

TABLE 8. FLIGHT LIMITATIONS

IAS Knots	120	150	180	210	250	290	320
Aircraft Q (psf) = Extended Probe Pd_y	49	76	110	150	212	285	X
Short Probe Pd_y = 0.79 Q	39	60	87	118	167	225	275
Flow Angle Limits (deg) Extended and Short	38	24	17	12	8	6	5

The airspeed limits are 320 and 290 knots IAS for the short and long probe configurations respectively. The short probe can tolerate a higher airspeed because the aerodynamic influence of the nose of the canister reduces the sensed dynamic pressure. Most cloud physics research aircraft make measurement runs at airspeeds considerably below these values. At airspeeds above about 200 knots, care will have to be exercised in limiting the flow angle excursions during the airborne tests, which will involve intentional pitching and yawing manoeuvers and cloud penetrations.

8.0 CONCLUSIONS

The 858-equipped canister has been wind tunnel tested and calibrated over the range of airspeeds and flow angles representative of the flight envelope of the Twin Otter. The probe has been tested in a

short configuration for sensing airflow near the sampling plane of a PMS probe, and in an extended configuration, both to measure airflow well ahead of a PMS canister and to simulate the use of the 5-hole probe on the noseboom of the Twin Otter. The aerodynamic influence of the canister on the measured airspeeds and flow angles has been documented.

The 5-hole probe adequately measures airspeed without the necessity of correcting for off-axis flow at angles up to ±15 degrees. The expected reduction in dynamic pressure due flow angle effects on sensed total pressure appears to be compensated by matching reductions in static pressure. Experimentally determined factors to correct dynamic pressure and measured airspeed for canister effects have been determined and agree well with theoretical predictions.

At flow angles up to at least ±15 degrees, the angles of attack and sideslip can be calculated independently without the inclusion of cross-coupling terms. In both the short and long configurations, flow angle is linearly related to the differential pressure ratios, with angles measured to accuracies of 0.3 and 0.2 degrees respectively. It is felt that the relationships determined here will still apply at the higher speeds on other test aircraft.

Static pressures measured by the 5-hole probe are not as accurate as those sensed by a conventional static probe. In any case, when used on the noseboom of the Twin Otter, special flight tests will be required to correct for position errors due to probe effects, the nose of the aircraft and the upwash of the wing.

9.0 ACKNOWLEDGEMENTS

The author is indebted to A.M. Drummond for reviewing this manuscript and for his contribution of Appendix B. Appreciation is expressed to R.J. Templin, Head of the Low Speed Aerodynamics Section of NAE, for the use of the 6 × 9 tunnel for these tests, and to T.R. Brown, J. Pye and R. DuFault for operation of the tunnel and initial processing of the tunnel test data.

10.0 REFERENCES

Baumgardner, D., 1984: The Effects of Airflow Distortion on Aircraft Measurements - A Workshop Summary. Bulletin of the American Meterological Society, 65, 1212-1213.

Brown, E.N., C.A. Friehe and D.H. Lenschow, 1983: The Use of Pressure Fluctuations on the Nose of an Aircraft for Measuring Air Motion. Proceedings of the Fifth Symposium on Meteorological Observations and Instrumentation, April 11-15, 1983, Toronto, Ontario.

Drummond, A.M., 1977: Effects of Aerodynamic Interference on the Atmospheric Environment Service Particle Measuring Devices on the NAE Twin Otter. NRC, NAE Laboratory Technical Report LTR-FR-59.

Drummond, A.M., 1983: The Shedding of Drops and Ice from the Twin Otter Propellers to the AES Probes. NRC, NAE Laboratory Technical Report LTR-FR-85.

Drummond, A.M., 1984: Aircraft Flow Effects on Cloud Droplet Images and Concentrations. NRC, NAE Aeronautical Note NAE-AN-21.

Drummond, A.M. and J.I. MacPherson, 1984: Theoretica and Measured Airflow about the Twin Otter Wing. NRC, NAE Aeronautical Note NAE-AN-19.

Drummond, A.M. and J.I. MacPherson, 1985: Aircraft Flow Effects on Cloud Drop Images and Concentrations Measured by the NAE Twin Otter. Paper submitted to the American Meteorological Society Journal of Atmospheric and Oceanic Technology.

Isaac, G.A., J.W. Strapp, R.S. Schemenauer and J.I. MacPherson, 1982: Summer Cumulus Cloud Seeding Experiments near Yellowknife and Thunder Bay, Canada. Journal of Applied Meteorology, 21, 1266-1285.

Kaushagen, W.M., 1949: Flight Line Computer. Cornell Aeronautical Laboratory Report IH-431-P-28.

Kuethe, A.M. and J.D. Schetzer, 1950: Foundations of Aerodynamics, Wiley and Sons, 374 pp.

MacPherson, J.I., J.M. Morgan and K. Lum, 1981: The NAE Twin Otter Atmospheric Research Aircraft. NRC, NAE Laboratory Technical Report LTR-FR-80.

Ower, E. and R.C. Pankhurst, 1977: The Measurement of Airflow. Pergamon Press, 363 pp.

Streeter, V.L., 1971: Fluid Mechanics. McGraw-Hill Company, 755 pp.

FIG. 1: THE NAE TWIN OTTER ATMOSPHERIC RESEARCH AIRCRAFT
SHOWING THE AES-OWNED PMS PROBES

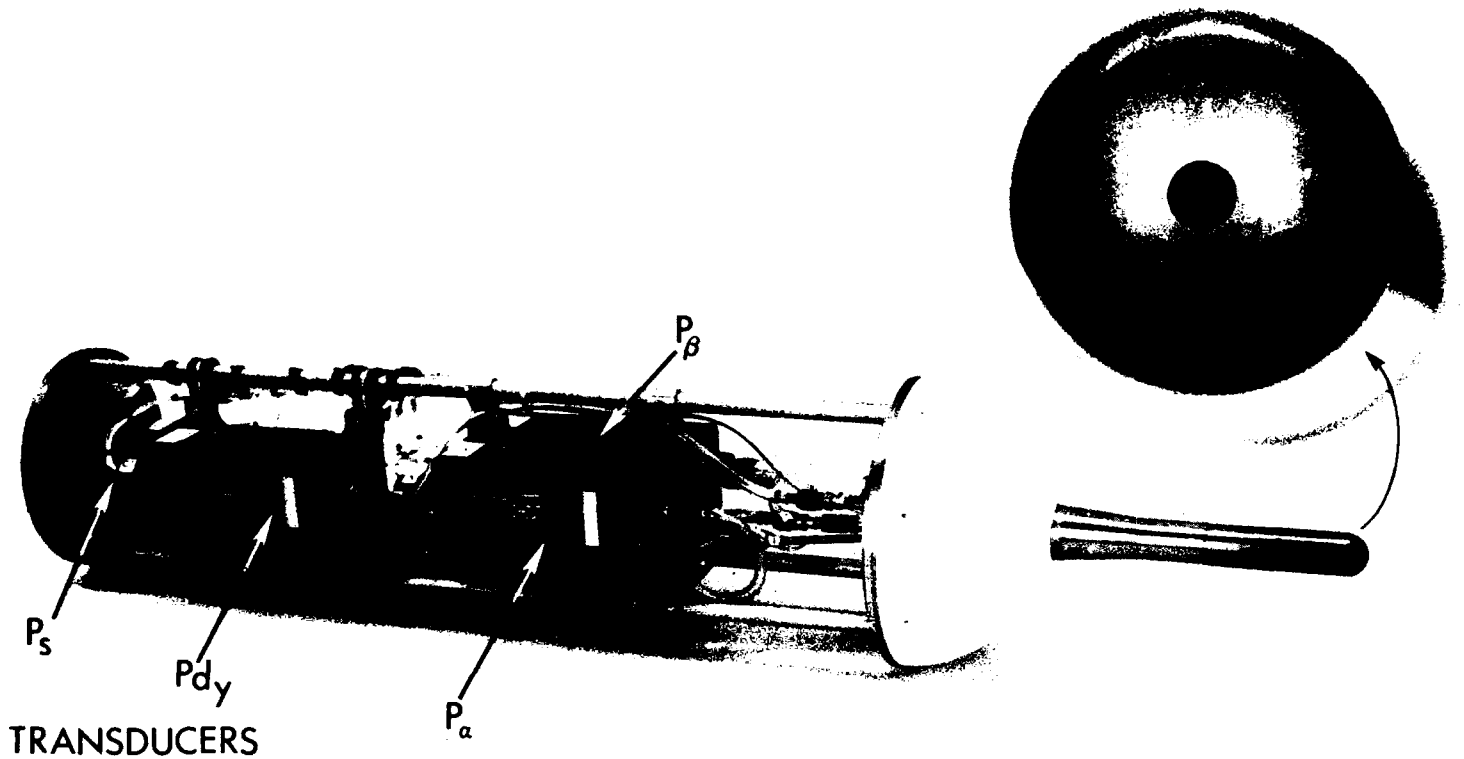

FIG. 2: THE INSTRUMENTED CANISTER AND 5-HOLE PROBE

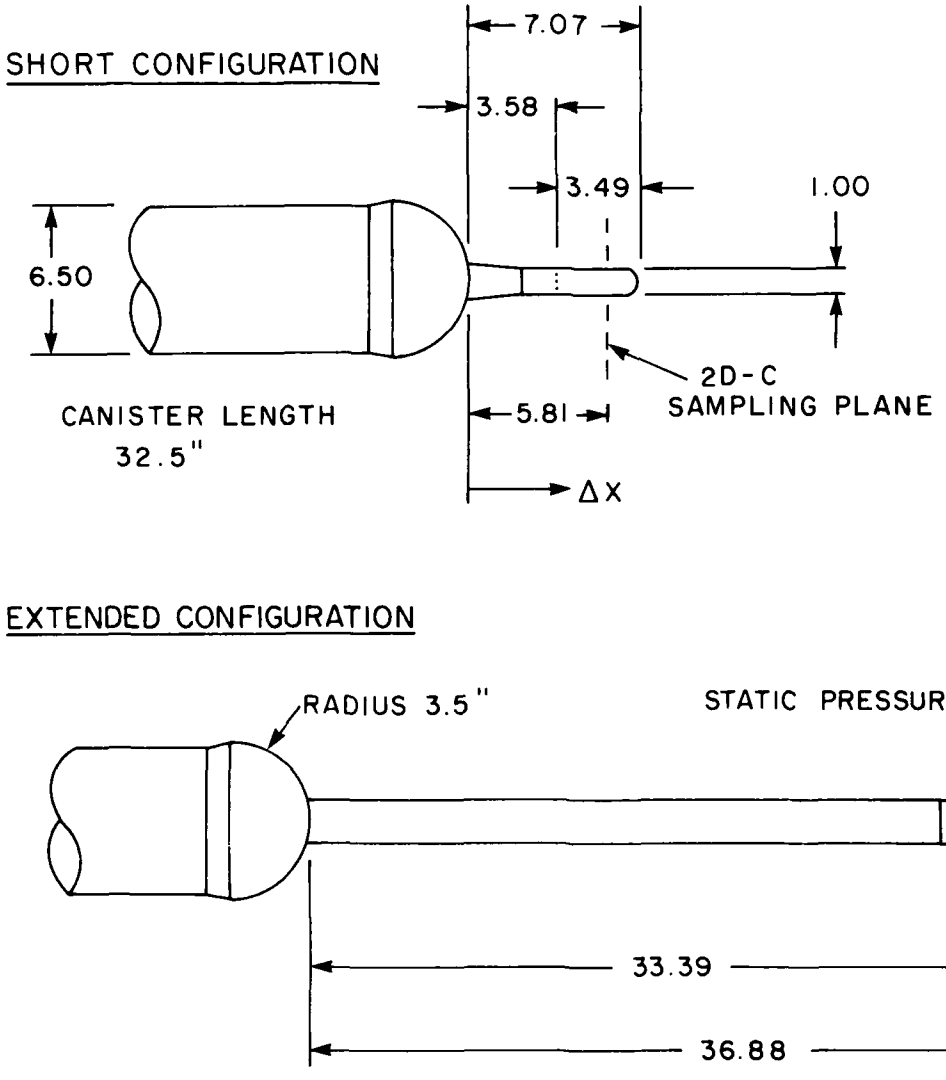

FIG. 3: SCHEMATIC AND DIMENSIONS OF THE PROBE IN THE SHORT AND EXTENDED CONFIGURATIONS

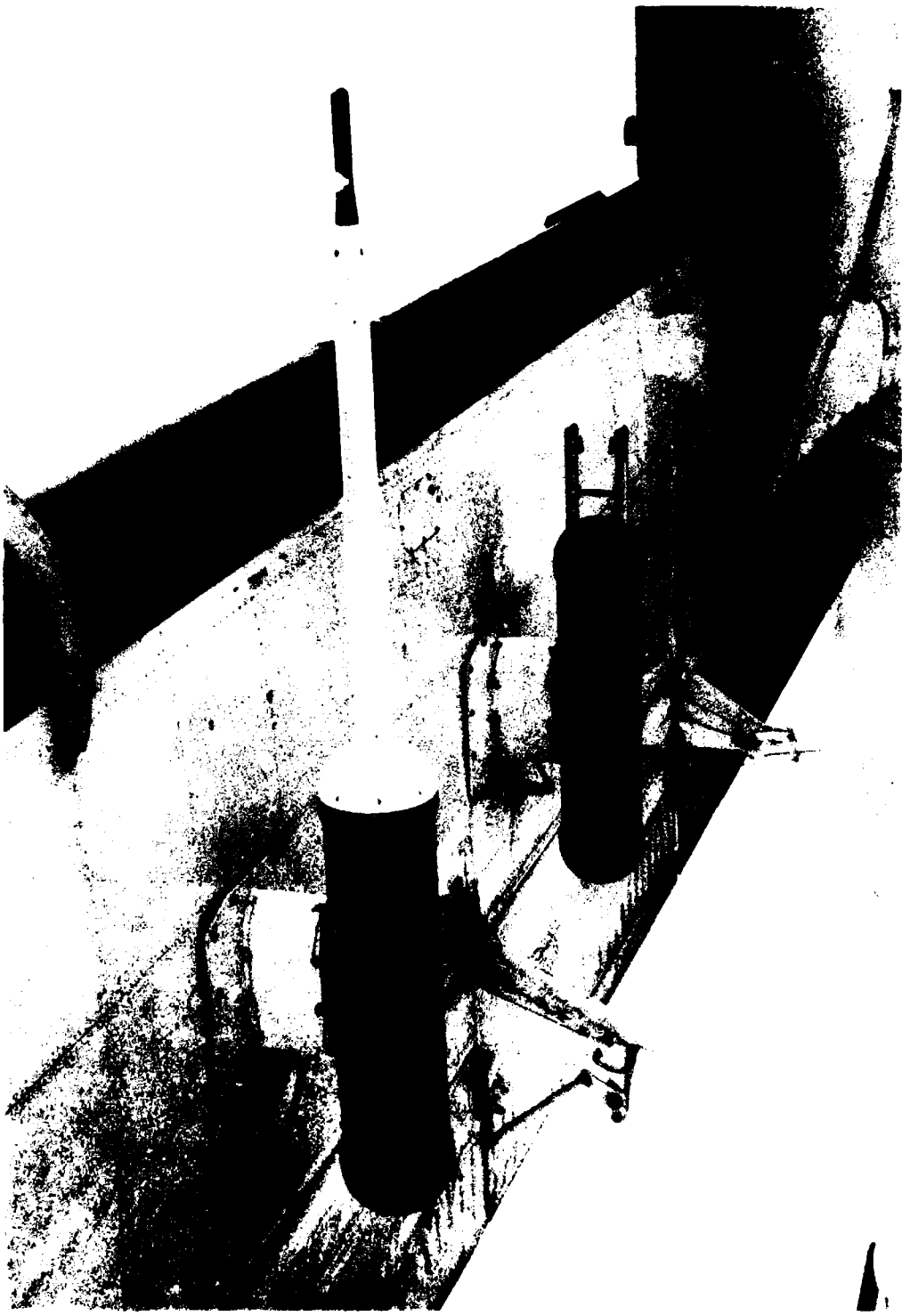

FIG. 4: EXTENDED PROBE ON OUTBOARD PYLON ON TWIN OTTER WING

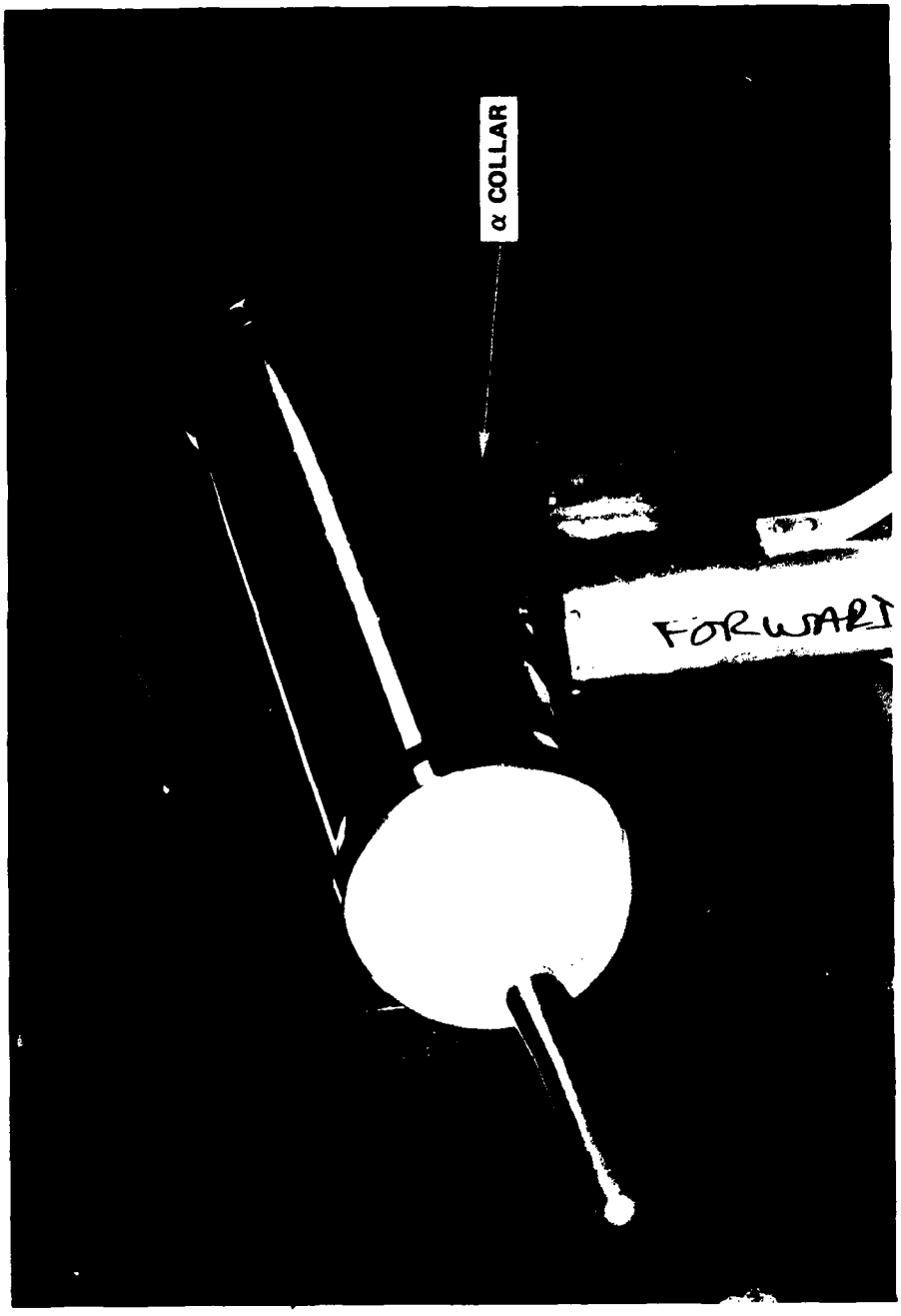

FIG. 5: THE SHORT PROBE IN THE WIND TUNNEL

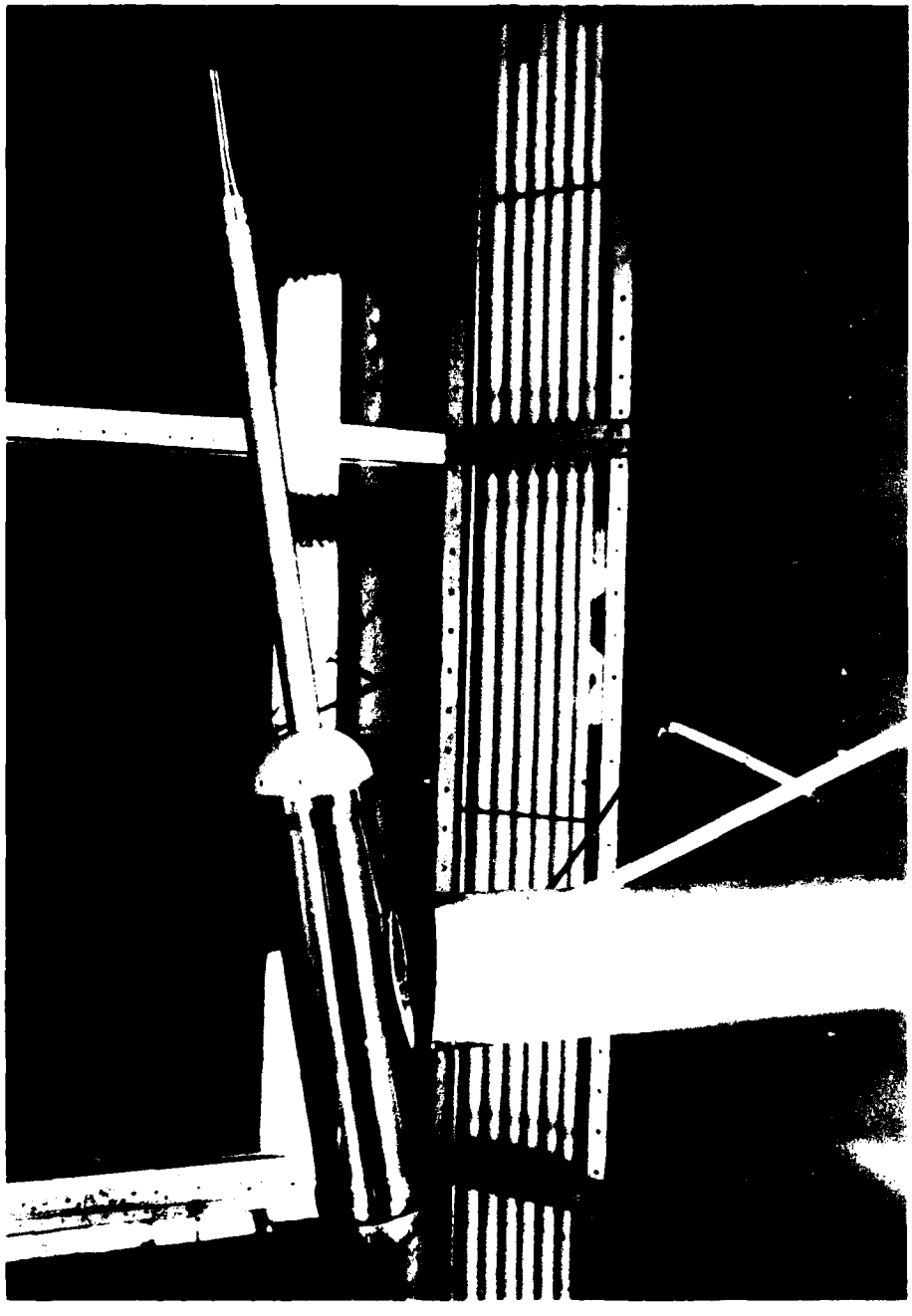

FIG. 6: THE EXTENDED PROBE IN THE WIND TUNNEL

RUN NUMBER 30 REPORT NUMBER 426 TARE NUMBER 27

PMS WITH EXTENDED PROBE

Q = 55, EXTENDED PROBE, ALPHA = 10 8

09-AUG-84 13:49:34 ATMOSPHERIC PRESSURE (KPA) 100.0

PT	ANGLE	VEL	ALF	RMS	BET	RMS	PDY	PST	TST
1	-14.0	220.6	46.27	1.34	-60.35	1.30	53.64	-4.48	-1.06
2	-12.0	220.5	46.80	1.57	-52.56	1.23	54.63	-3.99	-1.13
3	-10.0	220.5	47.27	1.40	-44.54	1.09	54.97	-3.16	-1.29
4	-8.0	220.5	48.10	1.39	-36.31	1.41	54.83	-2.11	-1.37
5	-6.0	220.5	48.21	1.31	-27.22	1.32	54.78	-1.11	-1.41
6	-4.0	220.5	47.48	1.28	-18.92	1.19	54.80	-0.29	-1.43
7	-2.0	220.7	47.64	1.24	-10.14	1.17	54.82	0.24	-1.46
8	0.0	220.7	47.44	1.11	-1.06	1.06	54.78	0.40	-1.46
9	2.0	220.7	47.43	1.34	7.35	1.22	54.93	0.22	-1.46
10	4.0	220.7	47.40	1.20	16.56	1.06	55.00	-0.03	-1.47
11	6.1	220.8	46.47	1.05	25.68	1.20	55.13	-0.67	-1.45
12	8.0	220.7	46.53	1.03	33.73	1.22	55.13	-1.31	-1.42
13	10.0	220.6	45.62	1.19	42.47	1.30	55.08	-2.42	-1.39
14	12.0	220.7	44.35	1.25	50.73	1.05	54.63	-3.46	-1.32
15	14.0	220.7	43.55	1.00	58.73	1.07	53.72	-3.97	-1.18

FIG. 7: EXAMPLE PRINT OF WIND TUNNEL OUTPUT DATA

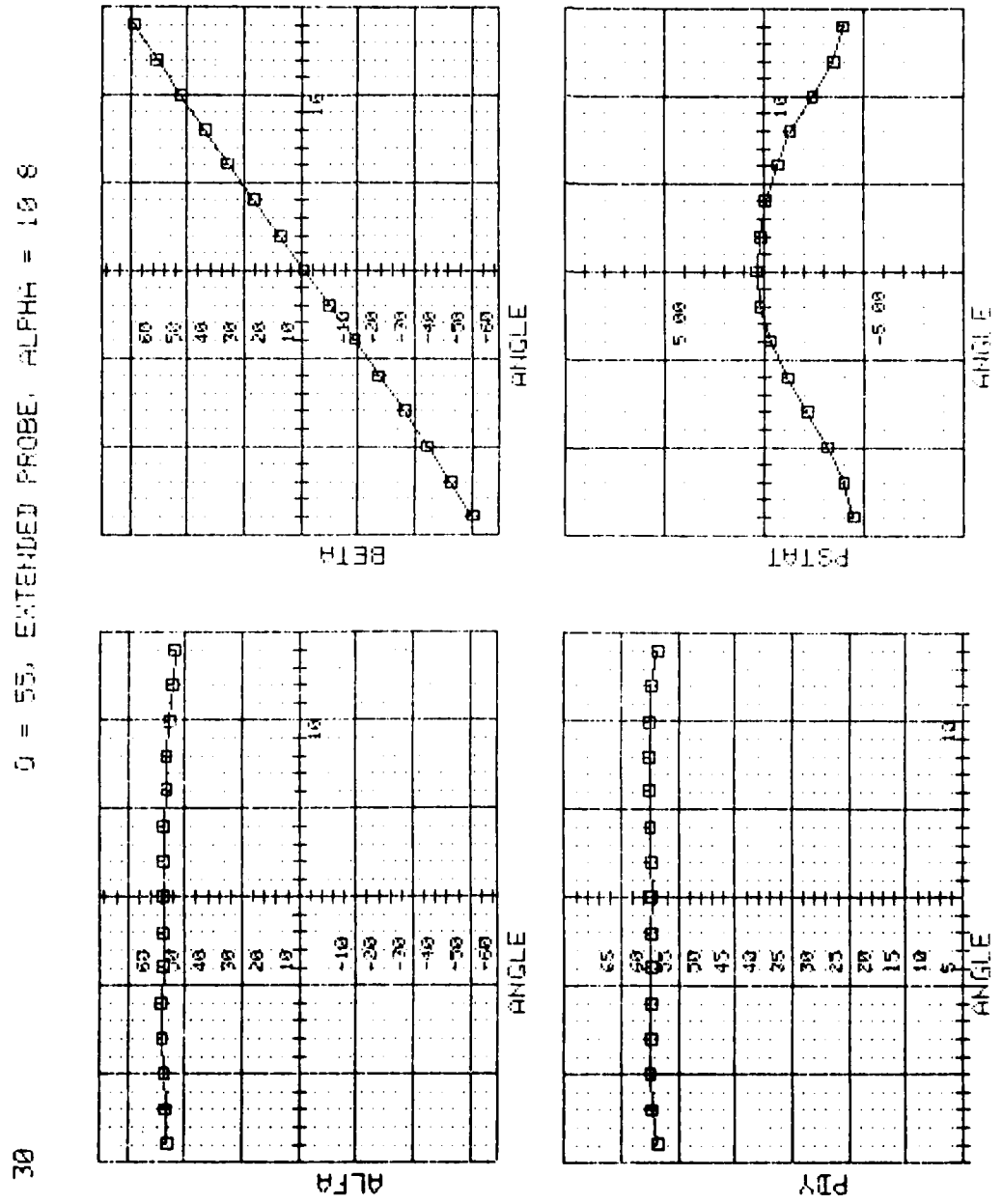

FIG. 8: EXAMPLE PLOTS OF WIND TUNNEL DATA

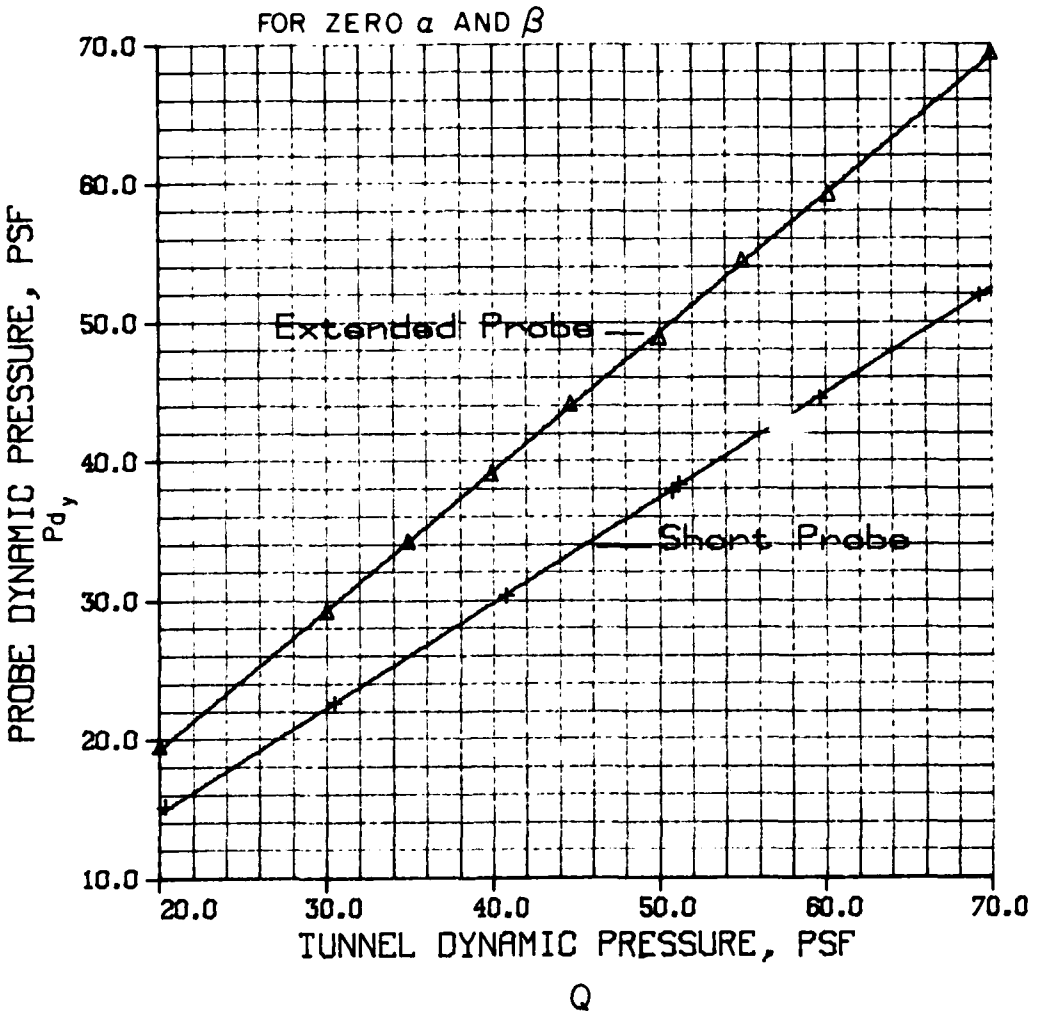

FIG. 9: PROBE vs TUNNEL DYNAMIC PRESSURE

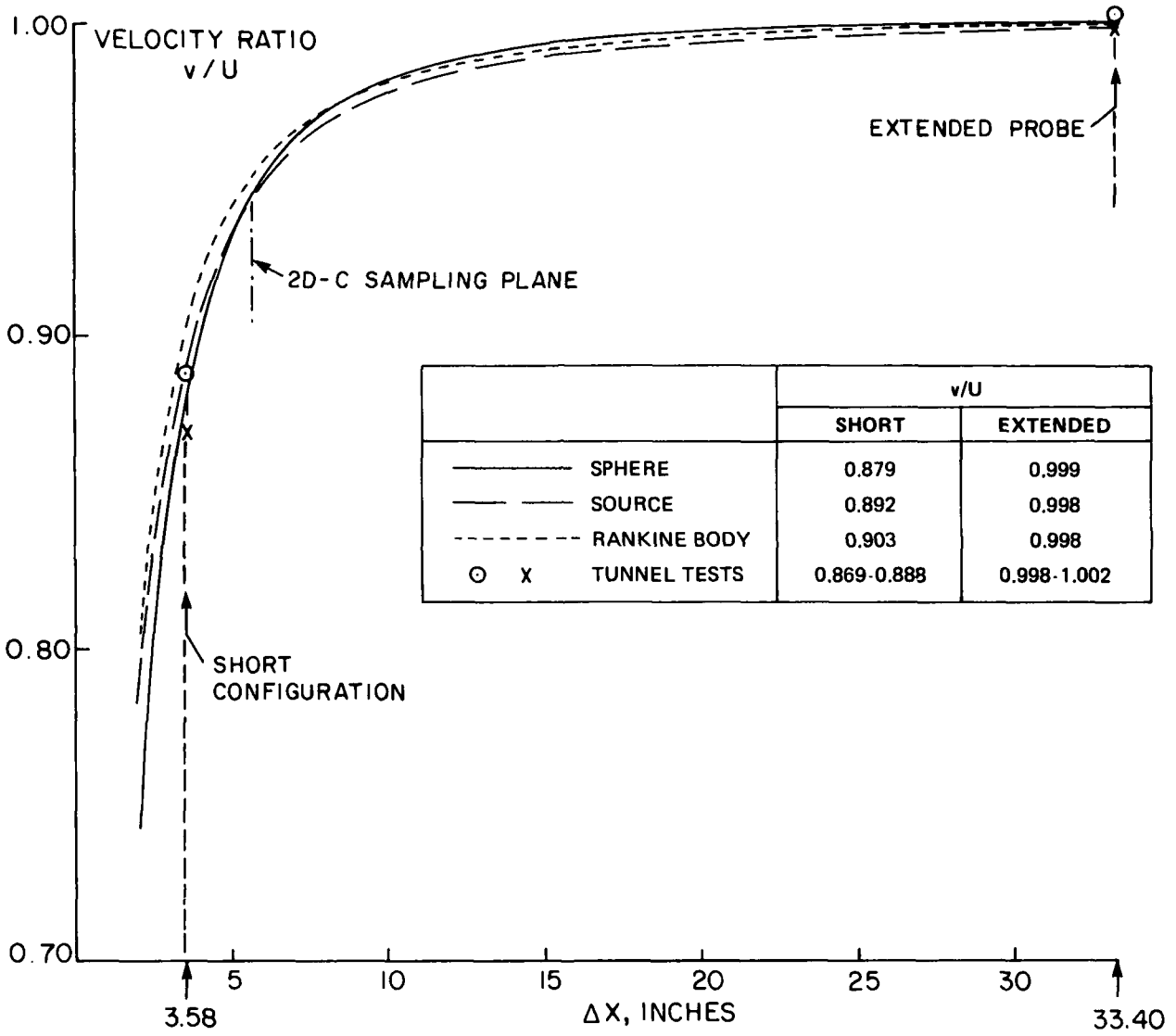

	v/U	
	SHORT	EXTENDED
SPHERE	0.879	0.999
SOURCE	0.892	0.998
RANKINE BODY	0.903	0.998
⊙ X TUNNEL TESTS	0.869-0.888	0.998-1.002

FIG. 10: PREDICTED AND MEASURED VELOCITY RATIOS

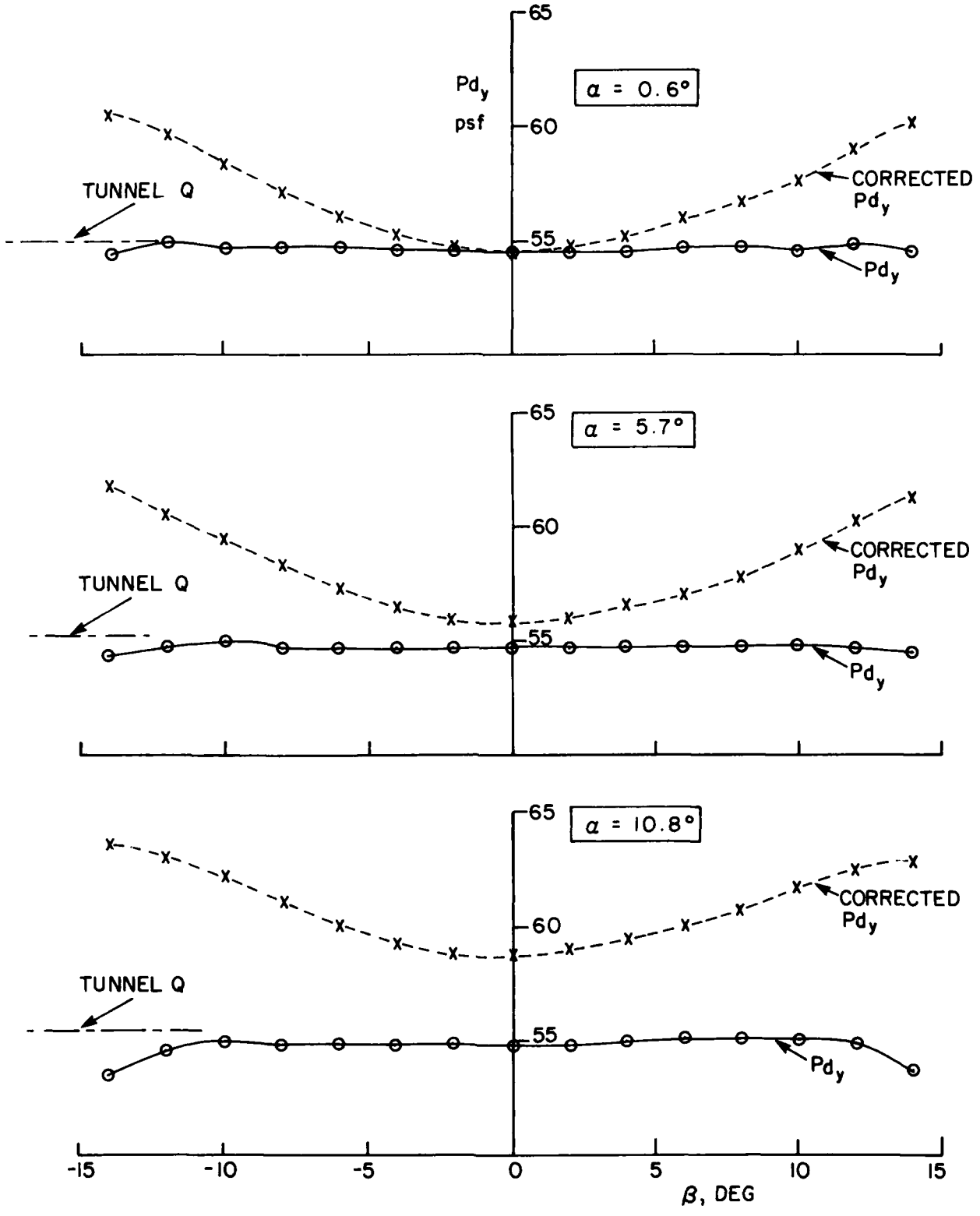

FIG. 11: EFFECTS OF CORRECTING Pd_y FOR FLOW ANGLE

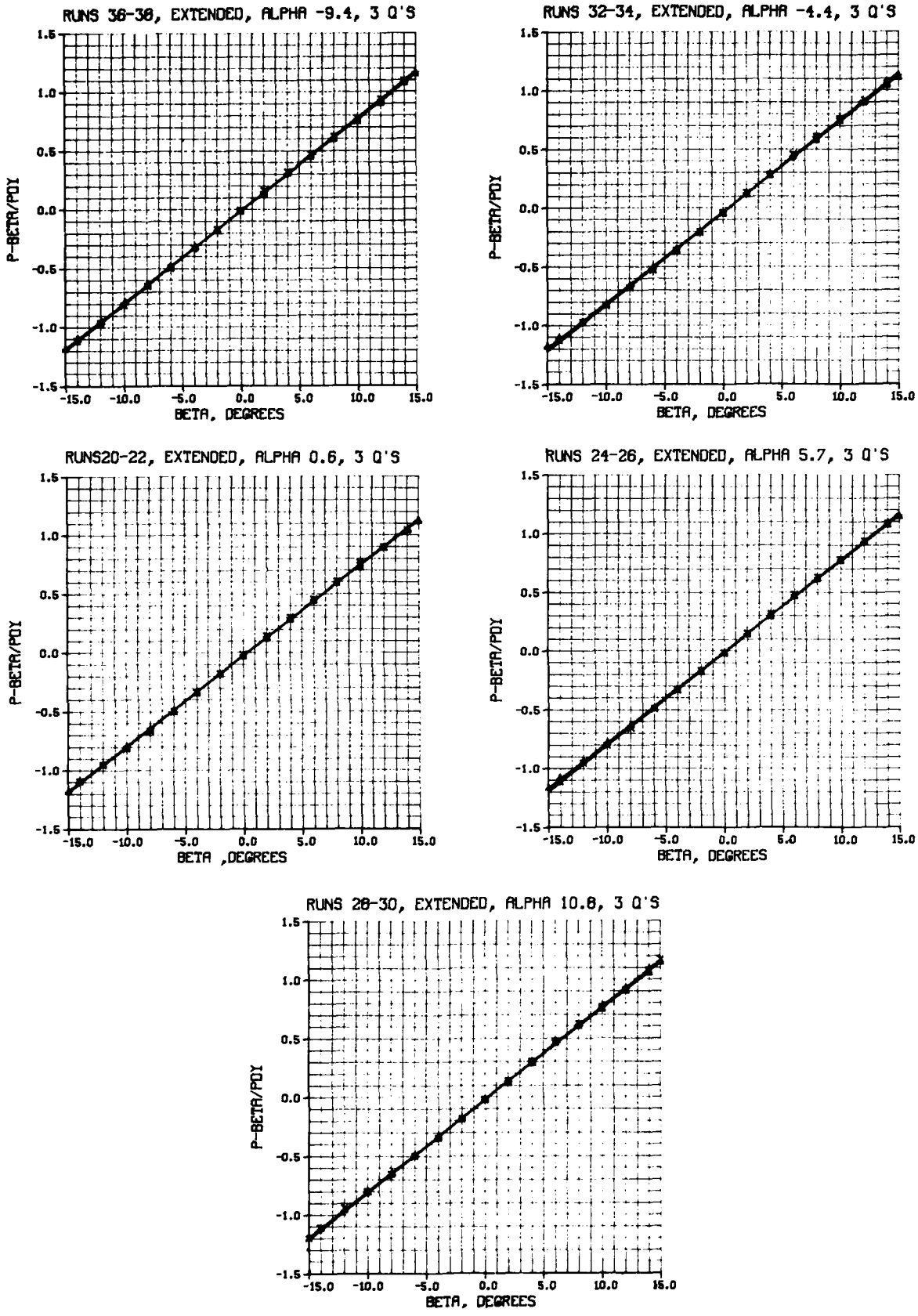

FIG. 12: EXTENDED PROBE FLOW ANGLE DATA

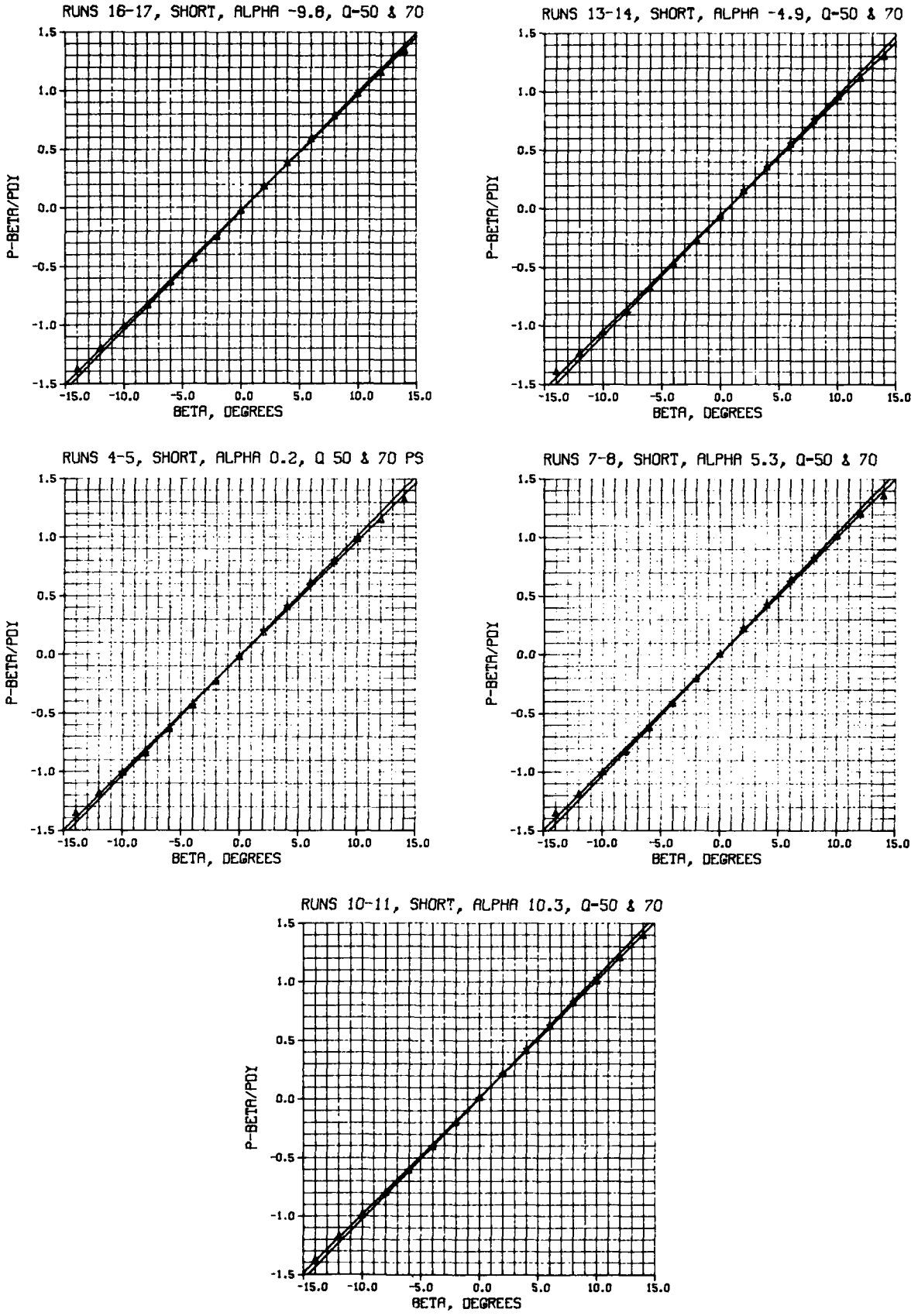

FIG. 13: SHORT PROBE FLOW ANGLE DATA

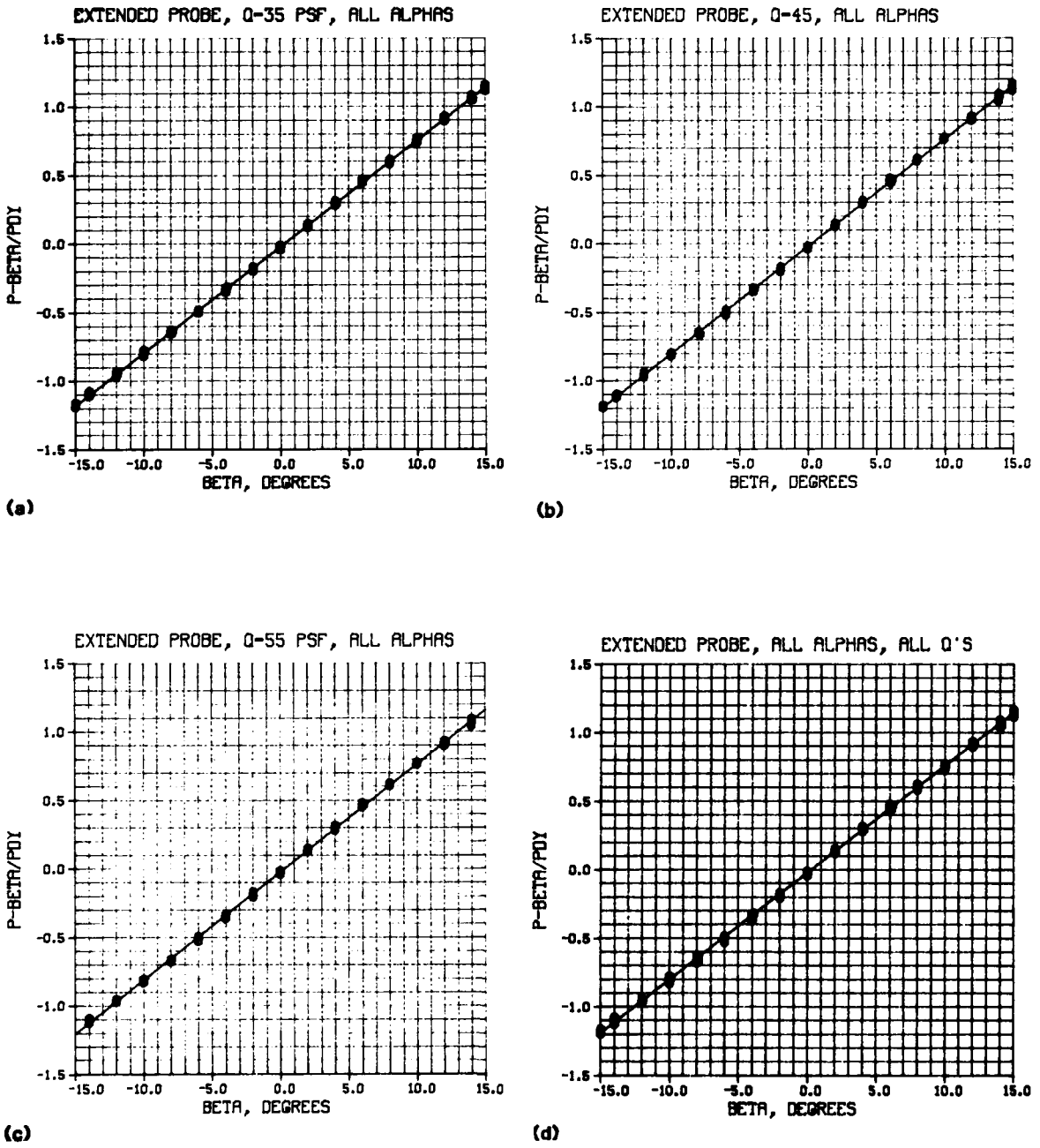

FIG. 14: EXTENDED PROBE FLOW ANGLE DATA COMBINED FOR ALL ANGLES OF ATTACK

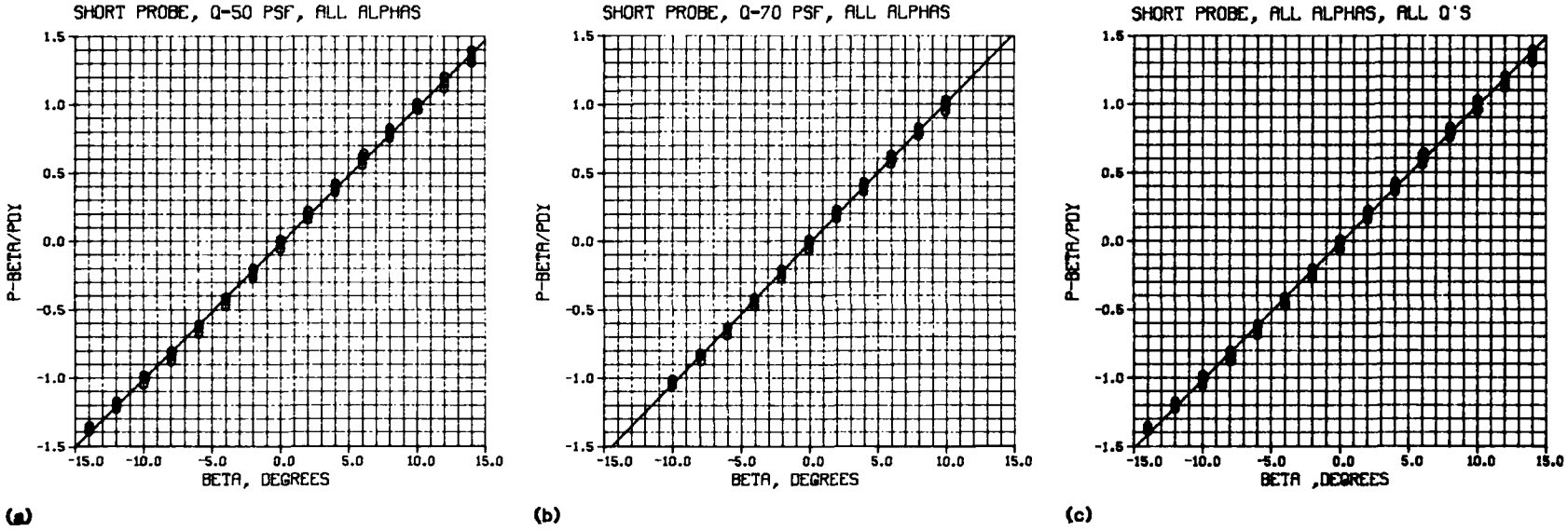

FIG. 15: SHORT PROBE FLOW ANGLE DATA COMBINED FOR ALL ANGLES OF ATTACK

APPENDIX A - CORRECTION TO DYNAMIC PRESSURE FOR OFF-AXIS FLOW ANGLES

When the stagnation point moves off the central pressure port on the 5-hole probe by angle α, the measured pressure would be expected to fall below the true dynamic pressure. From Equation (1) in Section 3.1:

$$Pd_y = P_3 - P_S = \tfrac{1}{2}\rho U^2(1 - \frac{9}{4}\sin^2\alpha) = Q(1 - \frac{9}{4}\sin^2\alpha) \qquad (A\text{-}1)$$

The approximation $1 - \frac{9}{4}\sin^2\alpha = \cos 2\alpha$ is accurate to within 2 per cent at angles up to 15 degrees. Hence:

$$Pd_y \approx Q\cos 2\alpha \qquad (A\text{-}2)$$

From Equation (6):

$$P_\alpha = \frac{9}{4} Q \sin 2\alpha \qquad (A\text{-}3)$$

and

$$P_\beta = \frac{9}{4} Q \sin 2\beta \qquad (A\text{-}4)$$

Considering first just the flow at angle α (β=0), squaring (A-3) and (A-2) and adding gives:

$$Pd_y^2 + \frac{16P_\alpha^2}{81} \approx Q^2(\sin^2 2\alpha + \cos^2 2\alpha) = Q^2 \qquad (A\text{-}5)$$

$$\text{and, } Q \approx \left(Pd_y^2 + \frac{16P_\alpha^2}{81}\right)^{\frac{1}{2}} \qquad (A\text{-}6)$$

For simulataneous α and β deflections, (A-2) would become:

$$Pd_y \approx Q\cos 2\alpha \cos 2\beta \qquad (A\text{-}7)$$

Squaring and adding (A-7), (A-3) and (A-4) produces:

$$Pd_y^2 + \frac{16P_\alpha^2}{81} + \frac{16P_\beta^2}{81} \approx Q^2(\cos^2 2\alpha \cos^2 2\beta + \sin^2 2\alpha + \sin^2 2\beta)$$

$$\approx Q^2(1 + \sin^2 2\alpha \sin^2 2\beta) \qquad \text{(A-8)}$$

$$\approx Q^2$$

to within 1.5 per cent for α and β both 10 degrees. Therefore:

$$Q \approx Pd_y \left[1+ \frac{16}{81} \left(\frac{P_\alpha}{Pd_y}\right)^2 + \frac{16}{81} \left(\frac{P_\beta}{Pd_y}\right)\right]^{\frac{1}{2}} \qquad \text{(A-9)}$$

Another approximation, valid at low Mach Numbers, is involved when Q is represented by $P_T - P_S$ or the measured Pd_y. From the isentropic flow equations in compressible flow (Kuethe and Schetzer, 1959):

$$\frac{P_T}{P_S} - 1 = \left(1+ \frac{\gamma - 1}{2} M^2\right)^{\frac{\gamma}{\gamma - 1}} - 1 \qquad \text{(A-10)}$$

Utilizing the binomial expansion for the bracketed expression yields:

$$P_T - P_S \approx P_S\left(\frac{\gamma}{2} M^2 + \frac{\gamma}{8} M^4 + \frac{(2-\gamma)}{48} M^6 \ldots\right) \qquad \text{(A-11)}$$

$$\text{But } Q = \tfrac{1}{2}\rho U^2 = \frac{\gamma}{2} P_S M^2 \text{ or } P_S = \frac{2Q}{M^2} \qquad \text{(A-12)}$$

and for air with $\gamma = 7/5$:

$$P_T - P_S = Q\left(1+ \frac{M^2}{4} + \frac{M^4}{40} \ldots\right) \qquad \text{(A-13)}$$

The tunnel tests were conducted at $M < 0.22$, so the approximation of using measured $P_T - P_S$ or Pd_y for Q is accurate to within one per cent.

APPENDIX B - THREE MODELS FOR THE FLOW FIELD AHEAD OF A PMS CANISTER

by A.M. Drummond

1.0 Introduction

It was desired to describe the flow about the canister of a Particle Measuring Systems (PMS) probe using classical hydrodynamic solutions because the spatial variation in the flow velocity in the vicinity of the canister could then be obtained from analytical expressions.

The canister has a cylindrical portion 25½ inches long with a diameter of 6.5 inches. At either end it has a hemispherical cap of 3.5 inches radius. The discontinuity at the joint of the cap and the cylindrical portion can not be modeled by simple classical methods. However, only the flow ahead of the canister along its axis of symmetry was desired, and no interest was to be paid to details of the flow aft of the canister stagnation point.

Three models for the canister were considered and each had certain attractive attributes. The first treated the canister as a sphere which accurately modeled the cap but ignored all effects of the canister aft of the discontinuity. The second treated the canister as a simple source, which did not treat the cap properly but did account for the finite width of the canister, at least asymptotically. The third treated the canister as a Rankine Body which correctly modeled the cylindrical portion and accounted for the finite length of the canister at the expense of an approximate treatment of the cap.

Each of the models will be described briefly and a numerical comparison of the axial velocity defect ahead of the cap will be given in the main body of the report.

Symbols used here are defined within the Appendix and are not necessarily consistent with those used in the main body of the report.

2.0 The Canister as a Sphere

A sphere of radius "a" in a uniform stream U with center at the origin is shown in Fig. B-1.

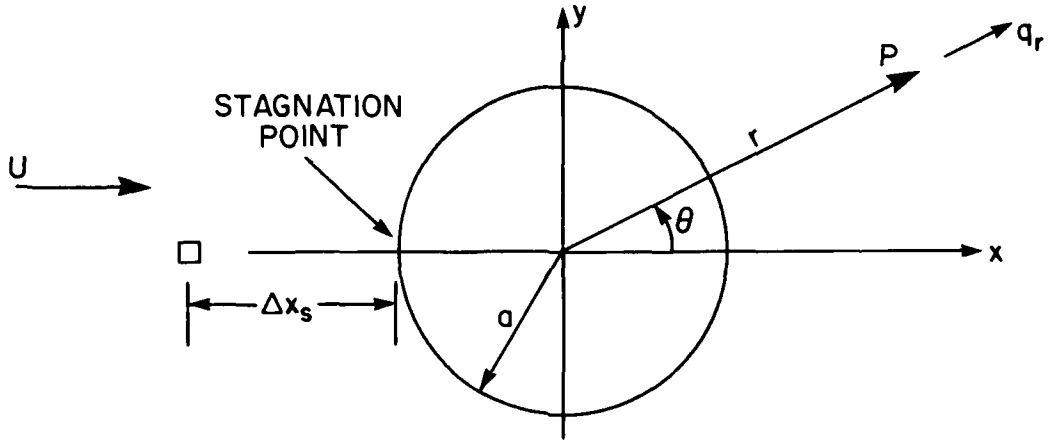

FIG. B-1

The point P is located by the co-ordinates r and θ and q_r is the velocity component in the radial direction. The stream function is (Milne-Thomson, p. 443):

$$\psi = -\frac{1}{2} U r^2 \sin^2 \theta \left(1-\left(\frac{a}{r}\right)^3\right) \qquad \text{(B-1)}$$

The velocity component q_r is given by:

$$q_r = -\frac{1}{r^2 \sin \theta} \frac{\partial \psi}{\partial \theta} \qquad \text{(B-2)}$$

Using ψ from Equation (B-1), the normalized radial velocity is given by:

$$\bar{q}_r = \frac{q_r}{U} = \cos \theta \left(1-\left(\frac{a}{r}\right)^3\right) \qquad \text{(B-3)}$$

To consider axial flow, the angle $\theta = \pi$. We define the point of interest to be Δx_s ahead of the stagnation point. The flow velocity in the positive x direction is:

$$\bar{q}_x = -\bar{q}_r = 1 - \left(\frac{a}{a+\Delta x_s}\right)^3 \qquad \text{(B-4)}$$

$$= 1 - \frac{1}{\left(1+ \frac{\Delta x_s}{a}\right)^3} \qquad \text{(B-5)}$$

The value of $\bar{q}_x$ is equal to 1 when $\Delta x_s = \infty$ and zero when $\Delta x_s = 0$.

3.0 The Canister as a Simple Source

A source placed at the origin in a uniform stream is shown in Fig. B-2 after Milne-Thomson, p. 437.

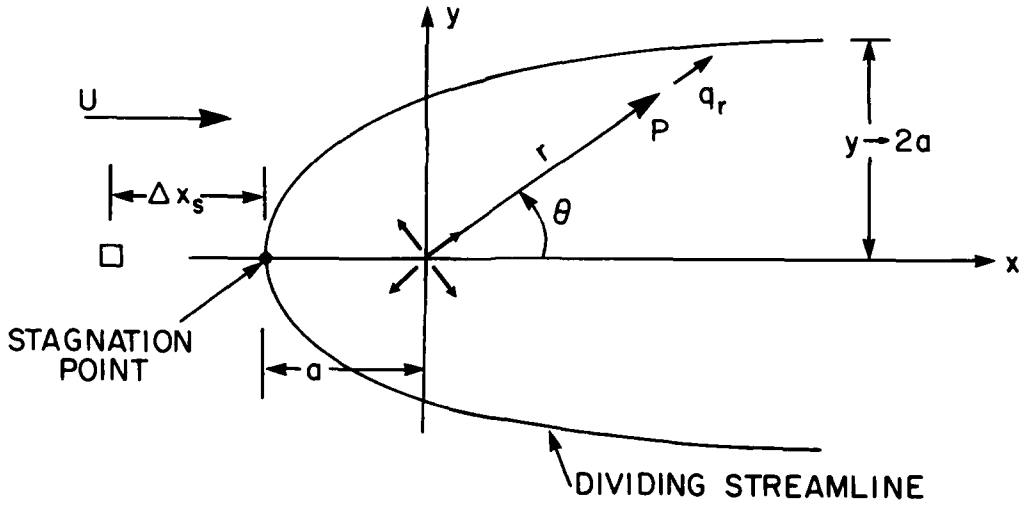

FIG. B-2

The stream function is:

$$\psi = -\frac{1}{2} U r^2 \sin^2\theta + m \cos\theta \qquad \text{(B-6)}$$

The value of m is chosen such that the stagnation point occurs when $\theta = \pi$ and $m = a^2U$. Using Equations (B-2) and (B-6), we write the expression for $\bar{q}_r$:

$$\bar{q}_r = \left[\cos\theta + \left(\frac{a}{r}\right)^2\right] \tag{B-7}$$

When $\theta = \pi$, and $\bar{q}_x = -\bar{q}_r$, the result is:

$$\bar{q}_x = 1 - \left(\frac{a}{r}\right)^2 \tag{B-8}$$

$$= 1 - \frac{1}{\left(1+\frac{\Delta x_s}{a}\right)^2} \tag{B-9}$$

The value of "a" is obtained from the asymptotic value of y when $r \to \infty$ and $\theta \to 0$, because $y \to R$ (the body radius) which equals 2a in the limit. Equation (B-9) is rewritten in terms of R as:

$$\bar{q}_x = 1 - \frac{1}{\left(1+\frac{2\Delta x_s}{R}\right)^2} \tag{B-10}$$

4.0 The Canister as a Rankine Body

The Rankine Body is discussed in Milne-Thomson (p. 441). There is a source at the point +e (Fig. B-3) and a sink at the point -e.

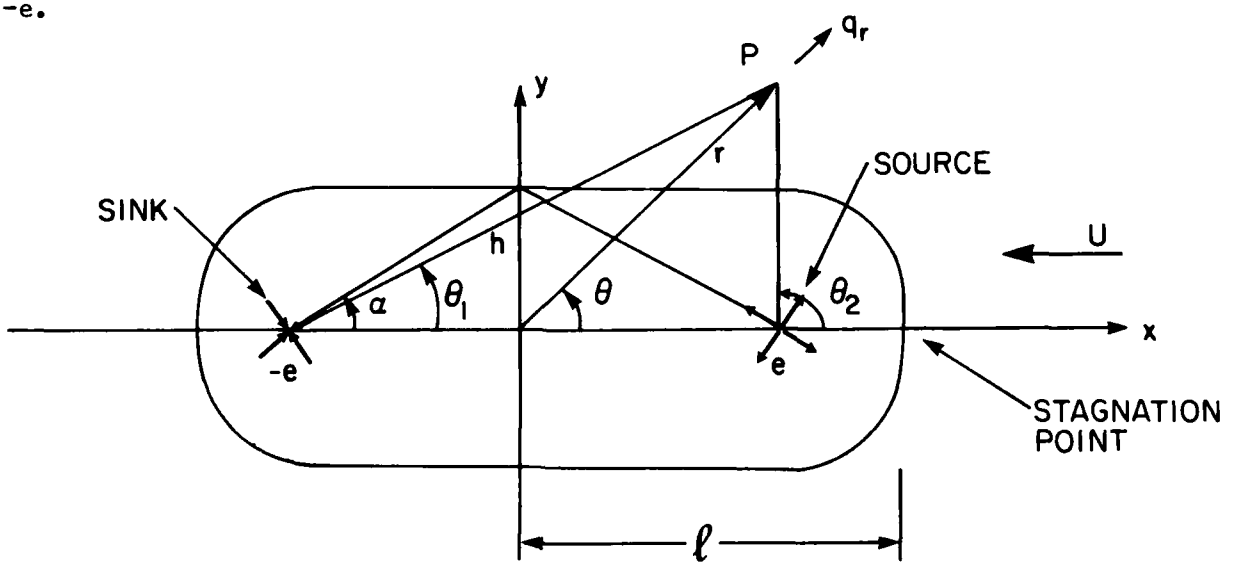

FIG. B-3

The fineness ratio F is defined as:

$$F = \frac{\text{length}}{\text{diameter}} = \frac{\ell}{h} \tag{B-11}$$

The stream function at a point P is given by:

$$\psi = \frac{1}{2} Ur^2 \sin^2\theta + m(\cos\theta_2 - \cos\theta_1) \qquad \text{(B-12)}$$

where θ_1 is the angle between the x axis and a line joining P to -e. Similarly, θ_2 is the angle between the x axis and a line joining P to e.

At the point x = 0, y = h on the body, the polar co-ordinates have the values:

$$r = h$$
$$\theta = \pi/2$$

and the variables in Equation (B-12) can be written:

$$\psi = 0$$
$$\theta_1 = \alpha$$
$$\theta_2 = \pi - \alpha$$

Hence, from Equation (B-12):

$$0 = \frac{1}{2} Uh^2 - m\ 2\cos\alpha \qquad \text{(B-13)}$$

Solving for m we get:

$$m = \frac{Uh^2}{4\cos\alpha} \qquad \text{(B-14)}$$

Set

$$m = \frac{b^2 U}{2} \qquad \text{(B-15)}$$

Therefore:

$$b^2 = \frac{h^2}{2\cos\alpha}$$

$$= \frac{h^2}{2e} \sqrt{e^2+h^2} \qquad \text{(B-16)}$$

From Fig. B-3:

$$\cos\theta_2 = (r\cos\theta - e)/\sqrt{r^2+e^2-2\,er\cos\theta}$$
$$\cos\theta_1 = (r\cos\theta + e)/\sqrt{r^2+e^2+2\,er\cos\theta} \qquad \text{(B-17)}$$

Finally, the stream function can be written:

$$\psi = \frac{1}{2}Ur^2\sin^2\theta + \frac{b^2U}{2}\left(\frac{(r\cos\theta - e)}{\sqrt{r^2+e^2-2\,er\cos\theta}} - \frac{(r\cos\theta + e)}{\sqrt{r^2+e^2+2\,er\cos\theta}}\right)$$

$$= \frac{1}{2}Ur^2\sin^2\theta + \frac{U}{2}\,\frac{h^2}{2e}\,\sqrt{e^2+h^2}\left(\frac{(r\cos\theta - e)}{J} - \frac{(r\cos\theta + e)}{K}\right) \qquad \text{(B-18)}$$

where

$$J = \sqrt{r^2+e^2 - 2er\cos\theta}$$
$$K = \sqrt{r^2+e^2 + 2er\cos\theta} \qquad \text{(B-19)}$$

We use the stagnation point condition to set the position of the source and sink inside the body.

Using the definition of $\bar{q}_r$, Equation (B-18) and the simplifying notation of (B-19), we have, after some lengthy algebra:

$$\bar{q}_r = -\cos\theta + \frac{h^2}{4e}\sqrt{e^2+h^2}\left[\frac{(r-e\cos\theta)}{J^3} - \frac{(r+e\cos\theta)}{K^3}\right] \qquad \text{(B-20)}$$

$$\bar{q}_\theta = \sin\theta\left[1 + \frac{h^2}{4}\sqrt{e^2+h^2}\left(\frac{1}{J^3} + \frac{1}{K^3}\right)\right] \qquad \text{(B-21)}$$

When $\theta = 0$ and $r = \ell$, a stagnation point exists at the nose of the Rankine body:

$$\bar{q}_\theta = 0$$

$$\bar{q}_r = 0 = -1 + h^2 \sqrt{e^2+h^2}\left(\frac{\ell}{(\ell^2-e^2)^2}\right) \qquad \text{(B-22)}$$

Equation (B-22) is used to find e in terms of the fineness ratio F (Equation (B-11)). We define:

$$A = e/\ell \qquad \text{(B-23)}$$

and write Equation (B-22) in terms of A and F. With some re-arrangement, the result is:

$$F^3(1-A^2)^2 = \sqrt{1+A^2F^2} \qquad \text{(B-24)}$$

Solutions to Equation (B-24) for A as a function of F are best performed numerically using, for example, Newton's Method. The following table shows a few solutions.

F	A
2	.7281
3	.8277
4	.8728
5	.8989
7.5	.9330
10	.9499
15	.9666

From Equation (B-20), with $\bar{q}_x = \bar{q}_r$, and $\theta = 0$ for flow velocity along the x axis, the following relation can be written:

$$\bar{q}_x = 1 - \frac{1}{F^2}\sqrt{A^2 + \frac{1}{F^2}} \times \frac{\xi}{(\xi^2-A^2)^2} \qquad \text{(B-25)}$$

where

$$\xi = r/\ell \approx 1 + \frac{\Delta x_s}{\ell} \qquad \text{(B-26)}$$

Note that the origin for ξ is at the mid-point of the body which requires that ξ be greater than 1.

The PMS canister has F equal to 5 and ℓ equal to 16.25 inches.

Reference

Milne-Thomson, L.M., 1955: Theoretical Hydrodynamics, Third Edition, MacMillan.

REPORT DOCUMENTATION PAGE / PAGE DE DOCUMENTATION DE RAPPORT

REPORT/RAPPORT	REPORT/RAPPORT
NAE-AN-32	NRC No. 24922
1a	1b
REPORT SECURITY CLASSIFICATION CLASSIFICATION DE SÉCURITÉ DE RAPPORT	DISTRIBUTION (LIMITATIONS)
Unclassified	Unlimited
2	3

TITLE/SUBTITLE/TITRE/SOUS-TITRE

Wind Tunnel Calibration of a PMS Canister Instrumented for Airflow Measurement

4

AUTHOR(S)/AUTEUR(S)

J.I. MacPherson

5

SERIES/SÉRIE

Aeronautical Note

6

CORPORATE AUTHOR/PERFORMING AGENCY/AUTEUR D'ENTREPRISE/AGENCE D'EXÉCUTION

National Research Council Canada
7 National Aeronautical Establishment Flight Research Laboratory

SPONSORING AGENCY/AGENCE DE SUBVENTION

8

DATE	FILE/DOSSIER	LAB. ORDER COMMANDE DU LAB.	PAGES	FIGS/DIAGRAMMES
85-09			63	15
9	10	11	12a	12b

NOTES

13

DESCRIPTORS (KEY WORDS)/MOTS-CLÉS

1. Particle measuring systems
2. Particles (airborne) — measurement
3. Aircraft (research)
4. Wind tunnel testing

14

SUMMARY/SOMMAIRE

Measurements of cloud particle images and concentrations using laser spectrometers housed in pods mounted on the wings or fuselages of research aircraft can be affected by the distortion of the airflow about the aircraft. The Flight Research Laboratory has developed a pod with a Rosemount 858 5-hole probe and pressure transducers to measure airflow angles and velocities at typical mounting locations on cloud physics research aircraft. This report documents the results of an extensive wind tunnel calibration of this pod to determine the factors relating the differential pressure measurements to the flow angles and velocities, and in particular to account for the effects of the canister itself on these measurements.

15

END

FILMED

12-85

DTIC